A Geodynamic Deformation Model of the Chuandian Region of Southeastern Tibet, with Constraints from GPS Data, Faults and Low-velocity Zones

Yudong Sun[1], Wei Leng[2], and Jing Liu-Zeng[3]

[1]University of Science and Technology of China
[2]Laboratory of Seismology and Physics of Earth's Interior
[3]Institute of Geology, China Earthquake Administrator

November 24, 2022

Abstract

Southeastern Tibet is a key region for studying the tectonic evolution of Tibetan Plateau. The region is characterized by distributed faults, localized low-velocity zones (LVZs) in the mid-lower crust, and prominent clockwise rotation of GPS velocity field. End-member models have been proposed to explain the origin of this deformation pattern, including the block extrusion model highlighting the role of faulted shear zones, and the crustal flow model emphasizing the effect of a weak lower crust. Here we use a 3D visco-elasto-plastic finite element model to reproduce the instantaneous horizontal surface velocity and investigate the effects of active faults and LVZs on that. The results show that when only faults are included, the residual surface velocities between modeled and observed values are large at some locations overlying the LVZs; when only LVZs are included, the residual surface velocities along the Xianshuihe-Xiaojiang and Lijiang-Xiaojinhe faults, two major faults with relatively high slip rates, are significant. However, when both faults and LVZs are considered, the modeled surface velocities fit well with observed GPS velocities. Our results therefore demonstrate that a combination of fault-bounding block extrusion and crustal flow type of continuous deformation is required to explain the surface deformation. The model yields a high-resolution strain rate map which provides an improved understanding of Quaternary tectonics and seismic hazards. In order to reduce the residual velocities, the viscosity of LVZs is constrained as ~10-10 Pa·s. Our study also suggests that LVZs are probably partially molten, which explains the rheology, seismological, and magnetotelluric data.

1   **A Geodynamic Deformation Model of the Chuandian Region of**

2   **Southeastern Tibet, with Constraints from GPS Data, Faults and**

3   **Low-velocity Zones**

4   **Yudong Sun[1], Wei Leng[1, 2], Jing Liu-Zeng[3]**

5   [1]Laboratory of Seismology and Physics of Earth's Interior; School of Earth and Space

6   Sciences, University of Science and Technology of China, Hefei 230026, China.

7   [2]CAS Center for Excellence in Comparative Planetology, Hefei 230026, China.

8   [3]Institute of Surface-Earth System Science, Tianjin University, Tianjin 300027, China.

9   Corresponding authors: Yudong Sun (syd1997@mail.ustc.edu.cn)

10   **Key points:**

11   ● We investigate the effects of the faulted shear zones and low-velocity zones on the

12   horizontal GPS velocity field in SE Tibet

13   ● The block extrusion model and crustal flow model may be both required to explain

14   the tectonic activities

15   ● Low-velocity zones are mechanically weak and possibly partially molten

16

17

18

19

20 **Abstract**

21   Southeastern Tibet is a key region for studying the tectonic evolution of Tibetan

22 Plateau. The region is characterized by distributed faults, localized low-velocity zones

23 (LVZs) in the mid-lower crust, and prominent clockwise rotation of GPS velocity

24 field. End-member models have been proposed to explain the origin of this

25 deformation pattern, including the block extrusion model highlighting the role of

26 faulted shear zones, and the crustal flow model emphasizing the effect of a weak

27 lower crust. Here we use a 3D visco-elasto-plastic finite element model to reproduce

28 the instantaneous horizontal surface velocity and investigate the effects of active

29 faults and LVZs on that. The results show that when only faults are included, the

30 residual surface velocities between modeled and observed values are large at some

31 locations overlying the LVZs; when only LVZs are included, the residual surface

32 velocities along the Xianshuihe-Xiaojiang and Lijiang-Xiaojinhe faults, two major

33 faults with relatively high slip rates, are significant. However, when both faults and

34 LVZs are considered, the modeled surface velocities fit well with observed GPS

35 velocities. Our results therefore demonstrate that a combination of fault-bounding

36 block extrusion and crustal flow type of continuous deformation is required to explain

37 the surface deformation. The model yields a high-resolution strain rate map which

38 provides an improved understanding of Quaternary tectonics and seismic hazards. In

39 order to reduce the residual velocities, the viscosity of LVZs is constrained as $\sim 10^{20}$-

40 10^{21} Pa·s. Our study also suggests that LVZs are probably partially molten, which

41 explains the rheology, seismological, and magnetotelluric data.

42

1. Introduction

43

44   Southeast Tibet, a mosaic of the Songpan-Ganzi Terrane, Sichuan Basin,

45   Chuandian block, Shan-Thai Plateau, and the northern part of the Indochina block, is

46   located on the southeastern borderland of the Tibetan Plateau, situated between the

47   Burma subduction zone, Yangtze block and Sunda plate (Yin & Harrison, 2000; Pan

48   et al., 2004). SE Tibet is often regarded as one of the most tectonically-active regions

49   in the Asian continent (Figure 1a; Tapponnier et al., 1982, 2001; Wang, 1998; Deng et

50   al., 2003; Zhang et al., 2003). A large topographic relief has been formed with a

51   complex network of faults (Figure 1b; Clark & Royden, 2000; Liu-Zeng et al., 2008;

52   Tapponnier et al., 2001; Taylor & Yin, 2009). Large earthquakes (Mw 7 or 8) have

53   occurred in the region (Zhang & Liu, 1978; Chen & Wu, 1989; Xu et al., 2009; Xu et

54   al., 2013; Yin et al., 2019). In addition, Tertiary-Quaternary magmatic activities have

55   occurred in Tengchong (Wang et al., 2007), along the Red River fault (Wang et al.,

56   2001) and in other areas, accompanied by high heat flux in much of Yunnan Province

57   (Hu et al., 2000; Wang, 2001). As a result, the region has attracted much attention

58   from researchers in terms of the study of seismic hazards, and because of the

59   complexity of the geological systems.

60   A remarkable pattern of clockwise rotation of the horizontal velocity field around

61   the eastern Himalayan syntaxis (EHS) has been observed in SE Tibet from modern

62   geodetic measurements during the last few decades (Shen et al., 2005; Gan et al.,

63   2007; Wang et al., 2016; Zheng et al., 2017). The GPS velocities decrease roughly

64   with increasing radial distance from the EHS, and there are several large deformation

65   centers along several major active faults and inside the blocks. The dynamic

66 mechanism of this surface deformation is still debated. And its relationships with

67 geological structures, lithospheric rheology, and earthquake hazards are poorly

68 understood.

69   Two main models have been proposed to explain the origin of this deformation

70 pattern in SE Tibet: the block extrusion model (Tapponnier et al., 1982, 2001; Peltzer

71 & Tapponnier, 1988; Avouac & Tapponnier, 1993) and the lower crustal flow model

72 (Royden et al., 1997; Clark & Royden, 2000). In the extrusion model, the Shan-Thai,

73 Indochina, Chuandian and Songpan blocks are extruded outwards, step by step,

74 following the indention of the Indian Plate into the Eurasian Plate (Tapponnier et al.,

75 1982; Peltzer & Tapponnier, 1988). The clockwise eastward extrusion results from

76 the south-north shortening of central Tibet and the advance of the strong EHS (Panda

77 et al., 2018). Specifically, the "bookshelf" model (England & Molnar, 1990)

78 suggested that the deformation is conducted from the eastward extrusion to SE Tibet,

79 via block rotation and fault slipping. The Shan-Thai block perhaps exemplifies a

80 classic case of the "bookshelf" model (Wang, 1998; Tapponnier et al., 2001; Shi et al.,

81 2018), with a nearly parallel series of left-lateral faults and two right-lateral faults (the

82 Red River and Sagaing faults) on both sides (Figure 1b). Explicitly, the book-like

83 blocks rotate clockwise when the Red River and Sagaing faults slip dextrally.

84   In order to explain both the simultaneous extension and uplift of Tibet and the

85 surrounding highlands, such as the Songpan-Ganzi Terrane in SE Tibet (Liang et al.,

86 2013), several researchers have emphasized the flow of the low viscosity lower crust

87 as a channel, driven by Himalayan collision and the high-elevation topography of

88 Tibetan Plateau (Shen et al., 2005; Royden et al., 2008). In order to explain the

89 northeastern and southeastern shunting of extrusion, the lower crustal flow is thought

90 to be blocked by the strong Sichuan Basin (Clark and Royden, 2000; Cook & Royden,

91 2007). A lower crustal Poiseuille flow which is faster than the surface velocity can

92 explain the gentle slope of the topography across the Chuandian block but a steeper

93 slope across the margin of the Sichuan Basin (Clark & Royden, 2000; Clark et al.,

94 2005; Burchfiel et al, 2008). Furthermore, from recent high-resolution seismic

95 imaging (Yao et al., 2010; Bao et al., 2015), two low S-wave velocity zones (LVZs)

96 are observed at depths from 10 km to 40 km, which are interpreted as two localized

97 mid-lower crustal channel flows.

98   In addition to the block extrusion model and the lower crustal flow model, an

99 asthenospheric flow model has also been proposed to explain the clockwise rotation

100 (Becker & Faccenna, 2011; Magni et al. 2014; Huang et al., 2015; Sternai et al., 2016).

101 However, the perturbation of surface deformation of a smaller scale triggered by

102 asthenospheric flow may be much less than that triggered by faulted shear zones or

103 crustal flow, due to the greater depth of the asthenosphere and the possible decoupling

104 of lithosphere and asthenosphere (~100-200 km; Bendick & Flesch, 2013; Flesch et

105 al., 2018).

106   High-accuracy long-term horizontal GPS data can be used as the constraint to

107 evaluate the effects on the surface deformation pattern of either the fault network or

108 the crustal flow. Several previous geodynamic models have been proposed to explain

109 the velocity field in SE Tibet or across the whole of Tibet. The evolutionary models of

110   Tibet driven by the India-Eurasia convergence reproduce the clockwise rotation of the

111   horizontal velocity field in SE Tibet (Cook & Royden, 2008; Yang & Liu, 2009; Chen

112   & Gerya, 2016; Chen et al., 2017a). In order to obtain improved modeled velocity

113   profiles for comparison with observed GPS data, geodynamic models for SE Tibet (Li

114   et al., 2014; Zhu et al., 2016; Li et al., 2017b; Luo & Liu, 2018; Li et al., 2019b), or a

115   larger region (Chen et al., 2016; Tunini et al., 2017; Bischoff & Flesch, 2018, 2019;

116   Flesch et al., 2018) have been designed with imposed velocity boundary conditions.

117   These models include one or more key factors, such as faults, weak lower crust,

118   topographic gravitational energy, and block strength heterogeneities. In particular, Li

119   et al. (2017b) regarded the lower crust as a viscous sheet for the entire region with an

120   imposed fast velocity; however, this is contradicted by the localized LVZs revealed

121   by seismic tomography (Bao et al., 2015). In addition, the model of Bischoff & Flesch

122   (2018) includes the lower crustal flow in central Tibet constrained by seismic

123   tomography, and it provides a better fit to the GPS velocity data, except for SE Tibet.

124   Li et al. (2019b) suggested that gravitational spreading is the major cause of the

125   horizontal velocity field, but the viscosity of the upper crust used in their model is

126   relatively low (~0.8-4×10^{21} Pa·s). Therefore, a high resolution model of SE Tibet with

127   a more accurate structure of faults and LVZs is needed to determine a more precise

128   mechanism for the observed deformation pattern.

129   **2. Model setup**

130   **2.1. Geodynamic model**

131   We used a 3D visco-elasto-plastic finite element model (Figure 2a; Moresi et al.,

132   1996, 2003; Leng & Gurnis, 2011, 2015), including crustal and lithospheric

133   heterogeneities, faults, and LVZs, to reproduce the instantaneous horizontal surface

134   velocity and examine the effects of faulted shear zones and LVZs on that. The model

135   solves the three conservative equations of mass, momentum and energy, with

136   Boussinesq approximation and the infinite Prandtl number:

$$v_{i,i} = 0 \quad (1)$$
$$-p_{,j}\delta_{ij} + \tau_{ij,j} = \Delta\rho g \delta_{i3} \quad (2)$$
$$\rho C_p (\dot{T} + v_i T_{,i}) = (kT_{,i})_{,i} \quad (3)$$

137   Here, $v_i, p, \tau_{ij}, \Delta\rho, g, \rho, C_p, T, k$, and δ_{ij} are respectively the velocity vector, pressure,

138   deviatoric stress tensor, density anomaly, gravitational acceleration, density, specific

139   heat capacity at constant pressure, temperature, thermal conductivity, and the

140   Kronecker function. For simulation of viscoelastic deformation, we considered the

141   crust and mantle as a Maxwell fluid, as follows:

$$\dot{\varepsilon}_{ij} = \frac{1}{2G}\dot{\tau}_{ij} + \frac{1}{2\eta}\tau_{ij} \quad (4)$$

142   where $\dot{\varepsilon}, \dot{\tau}, \tau, G$, and η are respectively the tensors of strain rate, stress rate, stress,

143   shear modulus, dynamic viscosity, and i, j represent spatial indices.

144   We used a power law relation to describe the temperature-dependent viscosity of

145   the lithosphere (Karato & Wu, 1993), as follows:

$$\eta = \eta_0 \left(\frac{\dot{\varepsilon}_{II}}{\dot{\varepsilon}_0}\right)^{\left(\frac{1}{n}-1\right)} exp\left(\frac{E}{nR}\left(\frac{1}{T} - \frac{1}{T_0}\right)\right) \quad (5)$$

146   where $\eta_0, \dot{\varepsilon}_{II}, \dot{\varepsilon}_0$, n, E, R, T, and T_0 are respectively the reference viscosity, second

147   invariant of the deviatoric strain rate tensor, reference strain rate, strain exponent,

148   activation energy, gas constant, and absolute and reference temperatures (Table 1).

149   For diffusion creep within the asthenosphere (Karato, 2010), we used a constant

150   viscosity of 10^{19} Pa·s. In addition, the transition from viscous creep to failure can be

151   reproduced by strain weakening effects. The strain weakening and strain-rate

152   weakening effect (non-Newtonian creep) both lubricate the shear zones (Tackley,

153   2000), and may promote the change of deformation from a brittle to ductile style

154   within the fault zone (Niemeijer et al., 2010). In our model, the effect of plastic strain

155   weakening was incorporated by decreasing the yielding stress with the accumulation

156   of plastic strain (Poliakov & Buck, 1998; Leng & Gurnis, 2011, 2015), as follows:

$$\tau_f = \mu P + C \quad (6)$$

$$\mu = \mu_0 - \mu_0 min\left(1, \frac{\varepsilon_p}{\varepsilon_f}\right) \quad (7)$$

$$C = C_0 - (C_0 - C_f) min\left(1, \frac{\varepsilon_p}{\varepsilon_f}\right) \quad (8)$$

157   Here, $\tau_f, P, \mu, \mu_0, \varepsilon_p, \varepsilon_f, C_0, C_f$, and C are respectively the yield stress, pressure,

158   coefficient of friction, initial coefficient of friction, accumulated plastic strain,

159   reference plastic strain, initial cohesion, minimum cohesion, and cohesion (Table 1).

160   Different rheology profiles were set for the faulted shear zones and continental

161   lithosphere with or without a weaker mid-lower crust (Figure 2b). The strength profile

162   of the lithosphere without LVZs follows the crème-brûlée model (Kohlstedt et al.,

163   1995), and the initial frictional coefficient, initial and minimum cohesion of friction

164   (μ_0, C_0, and C_f) were set to 0.5, 40 MPa and 0.6 MPa, respectively (Table 1). For the

165   strength profile of the faulted shear zones, only the yield stress was changed (μ_0, C_0

166   and C_f were set to 0.001, 4 MPa and 0.6 MPa, respectively), suggesting a pre-existing

167   fracture zone, or the occurrence of fluid, partial melting or weak minerals within the

168   fault zone (Collettini et al., 2009; Niemeijer et al., 2010; Carpenter et al., 2011;

169   Lockner et al., 2011; Gao & Wang, 2014). Notably, the variation of viscosity with

170   depth for faulted shear zones is still temperature- and stress-dependent and therefore it

171   varies between faults. The strength profile for the lithosphere with LVZs follows the

172   jelly sandwich model (Kohlstedt et al., 1995), with a lower constant viscosity for the

173   LVZ (Figure 2b).

174   The 3D Cartesian model (Figure 2a; Table 1) covers the area of the rectangle

175   shown in Figure 3a by transverse Mercator mapping. We used 120×82×28 elements

176   with 108 particles initially deployed in each element for tracking the material

177   properties and strain history (Leng & Gurnis, 2011, 2015). Vertically, it is divided

178   into four layers: a sticky air layer of 20 km, crust layer, mantle lithosphere, and

179   asthenosphere layer down to the depth of 282 km. The density of the crust and mantle

180   was set to 2.7 g/cm^3 and 3.3 g/cm^3, respectively. The initial thermal structure is

181   controlled mainly by lithosphere thickness, as a linearized distribution of temperature

182   varying with depth within the lithosphere, and a constant temperature for the

183   asthenosphere.

184   The high topography of Songpan-Ganzi terrane can be reproduced by including

185   different depths of Moho and LAB (see section 2.2.1 for the details) and the sticky air

186   layer after the model reaches isostacy. Therefore, the lithospheric deformation can be

187   driven by the gravitational potential energy.

188   Since the tectonic force of continental plates is derived from within the

189   lithosphere rather than from the asthenosphere, we applied driving forces in the model

190   via imposed lateral boundary velocities in the lithosphere (see section 2.2.2 for an

191   explanation of how we obtained the imposed lateral boundary velocities from GPS

192   data). The boundary condition of horizontal velocities was applied to lithospheric

193   sections on the four lateral walls of the box, which are constant with depth due to the

194   large viscosity of the lithosphere. Free-slip boundary conditions were used at

195   asthenospheric sections.

196   **2.2. Input data from observations**

197   **2.2.1. Crustal and lithospheric thickness**

198   The Moho depth map used in our model is from Yang et al. (2020) (Figure 2c).

199   And the lithospheric thickness is from Litho 1.0 (Figure 2d; Pasyanos et al., 2014),

200   which were obtained by iterating to fit the surface wave dispersion curves; it is well

201   correlated with the distribution of elastic thickness (Audet & Bürgmann, 2011).

202   **2.2.2. GPS data**

203   396 interseismic GPS data from SE Tibet (black arrows in the rectangle in Figure

204   3a; Zheng et al., 2017) for 1991 to 2015 were used as the observed surface velocities

205   and were compared with the modeled surface velocities. Furthermore, the laterally

206   imposed velocity boundary condition in the lithosphere is a key factor influencing the

207   surface deformation pattern. Previous geodynamic models typically interpolated the

208   GPS data to predefined meshes on the lateral boundaries; however, the GPS stations

209   are sparsely distributed on the box boundaries (Figure 3a) which reduces the accuracy

210   of the interpolation. Therefore, we computed the lateral boundary velocities based on

211   the "Blocks" model (Meade & Loveless, 2009), by this method which considers more

212   geological structural information. In this way, we first constructed a closed block and

213   fault network (the thin black lines in Figure 3a) based on the fault system collected by

214 Taylor & Yin (2009) (purple lines in Figure 3b). We then used 2576 GPS data from

215 Zheng et al. (2017) to invert for the rotating rate of each block and backslip rate of

216 each fault. From these two sets of parameters, the lateral boundary velocities on the

217 margin of the study area were calculated and are shown in Figure 3b.

218 **2.2.3. Faults**

219 Our fault model for SE Tibet was constructed based on fault traces, earthquake

220 locations, and focal mechanisms (Figure 4a, 4b and 4c). Active faults in the Holocene

221 were compiled as a combination of several studies (Zhang et al., 2003; Taylor & Yin,

222 2009; Wu et al., 2018; Shi et al., 2018), and earthquake locations were used to

223 supplement the recognition of fault traces. Several faults with changes in strike were

224 simplified with segmented straight lines.

225 The dip angle of faults was inferred from seismic reflection profiles (Li et al.,

226 2010) and the focal mechanisms of recorded earthquakes occurring on the faults.

227 Records of focal mechanisms were collected from the Global CMT

228 (https://www.globalcmt.org; Ekström et al., 2012) and the China Earthquake Data

229 Center (http://data.earthquake.cn; Figure 4a), for 1966 to 2017. For each segment of a

230 fault, the dip angle was represented by the average rupture plane of adjacent

231 earthquake (distance < 20 km) and nearly parallel to the fault strike direction

232 (intersecting angle < 30°).

233 The fault locking depth was calculated following the method for determining the

234 seismogenic zone (Smith-Konter et al., 2011), which includes 95% of the total

235 earthquakes nearby (< 5 km), defining the boundary of seismic and aseismic zones.

236   Earthquake logs (Figure 4b) were downloaded from IRIS (http://ds.iris.edu/wilber3/,

237   from 1968 to 2018, with magnitude > 4) and the China Earthquake Data Center

238   (http://data.earthquake.cn, from 1968 to 2019, with magnitude > 2).

239   We used a finite-thickness weak zone to simulate the faulted shear zone,

240   following the examples of Hearn et al. (2002; 2009) and Johnson & Segall (2004).

241   Our fault model consists of a thin faulted shear zone of 11 km thickness above the

242   locking depth, and a thicker shear zone from the locking depth to the Moho,

243   representing the plastic creeping zone (Figure 4d). With regard to the upper part of the

244   faulted shear zone (i.e. above the locking depth), we set the dip angle as discussed

245   above; for the lower part (i.e. beneath the locking depth), we assumed that the dip

246   angle equals 90° (Figure 4d).

247   **2.2.4. Tomography of the LVZs**

248   Numerous studies of the seismic tomography of the crust and mantle structure in

249   SE Tibet have been conducted over the last decade, using different inversion methods

250   such as P waves (Wei et al., 2013; Yang et al., 2014; Huang et al., 2018), surface

251   waves (Chen et al., 2014; Wang et al., 2014; Bao et al., 2015; Wu et al., 2016; Shen et

252   al., 2016), and full waveforms (Chen et al., 2017b; Tao et al., 2018). With the

253   improved resolution of seismic imaging, two LVZs of both P and S waves in the crust

254   are illustrated in all models, although there are differences in detail between different

255   models. In general, one LVZ spreads from the Songpang-Ganzi Terrane, across the

256   Lijiang and Dali basins, to Western Yunnan; and the other extends along the

257   Xiaojiang fault and across the Red River fault to the Simao Terrane (Figure 5). These

258   two LVZs are spatially divided by the inner core of the Emeishan large igneous

259   province in Panzhihua-Xichang region (Chen et al., 2015).

260   Considering scale and resolution, we chose two models of S-wave tomography

261   for application in the study: Tao_2018 by full waveform inversion (Tao et al., 2018,

262   Figure 5a), and Shen_2016 by ambient noise inversion (Shen et al., 2016, Figure 5b).

263   The shapes of LVZs were contoured according to S-wave velocity anomalies. For

264   each depth, if the S-wave velocity anomaly was lower than a threshold, as $dVs/Vs <$

265    $-r*\sigma$, where r and σ are the ratio and standard deviation of velocity anomaly, it was

266   defined as an LVZ (Figure 5c and 5d). In addition, the low S-wave velocity layer

267   from 0 to 10 km provides information about the sediment layer within the Sichuan

268   Basin and therefore it was excluded from the model. Geophysical observations show

269   that these LVZs are characterized by low electrical resistivity (Bai et al., 2010), high

270   attenuation (Zhao et al., 2013), high Poisson's ratio (Chen et al., 2013; Sun et al.,

271   2014; Tao et al., 2018), and high heat flow (Hu et al., 2000). Low S-wave velocity

272   and a higher Poisson's ratio may indicate the presence of partial melting and the

273   reduction of viscosity (Takei, 2002; Brantut & David, 2018), and therefore in the

274   model we used the prescription that LVZs had a uniform lower viscosity, which was

275   later optimized in the modeling.

276   **3. Results**

277   **3.1. Impacts of faults and LVZs on surface deformation**

278   Both faulted shear zones and LVZs are regarded as "defects" in continents. The

279   strain resulting from screw dislocation of the planar "defect" is proportional to 1/r³,

280   where r is the distance from the "defect" to the observation location (Savage &

281   Burford, 1973; Okada, 1985; Landau & Lifshitz, 1986); therefore, we infer that the

282   impacts of faults and LVZs are limited to the area surrounding them. After applying

283   the velocity boundary conditions and gravitational potential energy, these "defects"

284   can be detected in GPS measurements by examining the residual velocity, which is

285   equal to the modeled velocity minus the observed velocity. We attempted to minimize

286   the residual velocity by testing scenarios of various geological settings in the

287   modeling, and the parameterizations with the best degree of fit were considered to be

288   estimates of the properties of the underground structure.

289   The residual velocity fields were computed when the model reached topographic

290   isostacy after stress relaxation. The distributions of the values of the root mean square

291   (RMS) of the residual velocity in five models are illustrated in Figure 6 and their

292   settings are specified in Table 2. In Figure 6a, the reference case (case_ref) without

293   faults and LVZs was unable to produce sufficient clockwise rotation at the Chuandian,

294   Western Yunnan and Simao Blocks, and there were relatively large residual velocities

295   across the entire area. When only faults were included into the model (case_fault,

296   Figure 6b), the residual velocities decreased significantly, but there were still some

297   areas with relatively large residual velocities. It is interesting to note that the

298   distribution of large residual velocities is similar to the distribution of two LVZs

299   (Ganzi, Lijiang, and Tengchong; Kunming, Chuxiong, and Simao). On the other hand,

300   when only LVZs with a viscosity of 10^{20} Pa·s were included into the model

301   (case_LVZs, Figure 6c), the remaining part with large velocity misfits occurred along

302   the Xianshuihe-Xiaojiang fault and Lijiang-Xiaojinhe fault, which are two active

303   shear zones with large slip rates. When both faults and LVZs were included in the

304   model, two cases (case_both1 and case_both2) where the LVZs are respectively

305   constrained by two different tomography models (Tao_2018 and Shen_2016 in Table

306   2) provide better fits of the surface motion in most locations (Figure 6d and 6e). The

307   results clearly demonstrate that faulted shear zones and localized LVZs are the two

308   most important factors, which jointly influence the velocity field in SE Tibet. Notably,

309   the model with only one factor exhibits poor GPS fitting at the location of the other

310   (Figure 6b and 6c).

311   **3.2. Estimating the structure and rheology of faults and LVZs**

312   We tried to provide a rough estimate of the thickness of the lower faulted zones,

313   using the model of faulted shear zones described above (section 2.2.3; Figure 4d).

314   Seismic and magnetotelluric data across the faults show that there are related weak

315   zones below the surface, but the thickness of these lower faulted zones are not well

316   constrained due to the low resolution and smearing effects of tomographic maps (Li et

317   al, 2019a; Yang & Duan, 2019). In case_fault (Table 2), when the thickness of the

318   lower faulted zone was increased from 11 km to 45 km, the RMS of the residual

319   velocity decreased rapidly at first, and then more slowly when the thickness of the

320   lower faulted zone reached ~22 km (Figure 7a). Therefore we estimate that the

321   thickness of the lower part of the faulted shear zone may be around 22 km for our

322   model, which reproduced the observed surface ground motion. Admittedly, There is

323   trade-off between the rheology and the thickness of faulted shear zones, and the yield

324   stress is not well constrained. Thus, this estimation may not indicate the actual

325   thickness of faulted shear zones.

326   In a similar way, we estimated the size and viscosity of LVZs, since they are

327   important to understand how the mid-lower crust deforms in response to tectonic

328   forces. Specifically, whether the LVZs (Figure 5a and 5b) are connected to each other

329   is greatly debated, due to the small-scale differences between the seismic tomography

330   results for SE Tibet (Wei et al., 2013; Bao et al., 2015; Shen et al., 2016; Huang et al.,

331   2018).

332   In case_both1 and case_both2, we first fixed the viscosity of the LVZs to 10^{20}

333   Pa·s and adjusted their size by changing the ratio r (defined in section 2.2.4). In

334   Figure 7b, the RMS of the residual velocity reaches a minimum value with the

335   volume of ~1.4-1.6×10^7 km^3. The resulting best fit models for Tao_2018 and

336   Shen_2016 are illustrated in Figure 5c and 5d, respectively. The RMS became very

337   large, as the size increased, two LVZs merged into one and the connections were wide

338   enough to conduct flow. Therefore, two LVZs are generally isolated, and it is unlikely

339   for the northwestern LVZ to flow southeastward to the other LVZ. Both best-fitting

340   results show a narrow connection between LVZs below the Chuxiong fault in the

341   southwest, but there is no connection at the shallow part (~10-km depth) at Xichang

342   in the northeast. Whether or not there is a connection in the lower part below Xichang

343   remains unclear, due to the difference in these two tomography models. With the size

344   of LVZs obtained in Figure 7b, the results of the RMS of the residual velocity versus

345   viscosity are illustrated in Figure 7c. It can be observed that in order to obtain the

346   minimum residual velocity, the viscosity for the LVZs needs to be within the range of

347   ~10^{20}-10^{21} Pa·s.

348   **3.3. Map of the strain rate**

349   In order to analyze the local tectonic processes in SE Tibet, we chose the ideal

350   model (case_both1, Figure 6d) and computed the first-order derivative of the velocity

351   field in order to obtain maps of the strain rate tensor, maximum shear strain rate,

352   extension strain rate, and vorticity (rotational strain rate) (Figure 8a, 8c, 9a and 9c,

353   respectively). They are compared with the corresponding strain maps (Figure 8b, 8d,

354   9b and 9d) which are smoothed by meshes of 0.2^{o} (latitudinal) by 0.25^{o} (longitudinal)

355   from the observed GPS data (Kreemer et al., 2014; lacking for the Sichuan Basin).

356   Essentially, our modeled strain rate maps successfully reproduced the observed

357   deformation pattern. The magnitude and direction of the strain rates approximate the

358   observed rates (Figure 8a and 8b), and the sense of strike-slip fault is consistent with

359   geological observations (Figure 9c and 9d).

360   Based on the magnitude of the clockwise rotation, SE Tibet can be divided into

361   three sub-regions (Figure 9c and 9d): (i)Northern Myanmar, the Sanjiang region, and

362   Western Yunnan; (ii) the Songpan-Ganzi Terrane, Chuandian Block, and the Simao

363   Terrane; (iii) the Sichuan Basin, South China, and the Sunda plate. The vorticity

364   decreases from the interior to the outside, bounded by the Litang-Chenghai-Longling-

365   Ruili fault and the Xianshuihe-Xiaojiang fault. The clockwise rotation of regions (i)

366   and (ii) is probably due to the east- to southeast-ward extrusion from Tibet, and the

367   anti-clockwise rotation of region (iii) may be due to extension resulting from the

368   Sunda or Pacific subduction (Shen et al., 2005).

369   In the extension strain rate map (Figure 9a and 9b), the model reveals extension

370   in the Chuandian block and compression in the Longmenshan region. It also

371   demonstrates staggered grids of extension and compression along several active faults,

372   such as the Xianshuihe-Xiaojiang fault, which possibly result from variable slip rate

373   along the fault. Several localized extensional zones may explain the formation of

374   basins such as the Tengchong, Dayingjiang and Ruili basins in Western Yunnan,

375   Lijiang, Jianchuan, Eryuan, Binchuan, and the Chenghai basins around the diamond-

376   shaped Lijiang-Dali block, Zhongdian and Litang basins (green outlines; Fgiure 9a

377   and 9b).

378   Distinct shear strain rates are evident along two chains of active faults in the

379   model (Figure 8c) and they match the observations (Figure 8d). One is the arcuate

380   Xianshuihe-Xiaojiang and Dien Bien Phu faults, and the other is the Lijiang-

381   Xiaojinhe, Longling-Ruili and Dayingjiang faults. In addition, in the Simao Basin, a

382   "tail" of shear deformation is evident extending westward from the curved

383   Xianshuihe-Xiaojiang fault (Figure 9c). Since no NE-trending faults coincide with the

384   high shear strain zone, it is possibly caused by the underlying LVZ.

385   Admittedly, the modeled maps do not exactly match the observed maps,

386   especially in terms of the magnitude of the maximum shear strain rate (Figure 8c).

387   This may be attributed to the smearing problem during the interpolation of the still

388   sparse GPS data (Figure 8d). For example, the modeled shear strain rates of the

389   Longriba, Litang and Nantinghe faults are much higher than the observed rates from

390 GPS. However, the higher shear strain rates shown by the model appear to be

391 compatible with geologic observations. For instance, the geological average slip rate

392 of the Longriba fault is 7.5 mm/yr during the latest Pleistocene and 2.1 mm/yr in the

393 Holocene (Ren et al., 2013); the slip rate on the Litang fault is 2.3 mm/yr during the

394 last 173 kyr (Chevalier et al., 2016) and 4 mm/yr in the last 14 kyr (Xu et al., 2005);

395 the Nantinghe fault slips is 4 mm/yr (Shi, 2014).

396 **4. Discussion**

397 Compared with previous models which simulate continental deformation, our

398 high-resolution model considers combined effects of different thicknesses of crust and

399 lithosphere, temperature-dependent non-Newtonian rheology, a realistic 3D fault

400 network, and tomography-based LVZs. Specifically, the heterogeneity of the strength

401 of different blocks can be reproduced by different thicknesses and temperature-

402 dependent rheology. The boundary condition is applied to the entire lithosphere using

403 horizontal velocities inverted from interseismic GPS data, and the isostatic

404 topography can be produced with a sticky air layer in our model. Therefore, our

405 lithosphere model is driven by both tectonic forces and topographic gravitational

406 potential energy. Admittedly, the boundary and initial conditions are still over

407 simplified; plus, the rheology, temperature, and density of the lithosphere are largely

408 unclear; and the structure and depth of faulted shear zones at greater depths are not

409 well constrained. Thus it was difficult to use the model to study the deformation of

410 deeper structure in detail. Notably, a perfect fit of GPS data is impossible and

411 therefore our intention is to study the major features in tectonics with the focus on the

412   factors controlling deformation.

4.1. Block extrusion model vs. lower crust flow model

414   The two prevailing models of the geodynamics of SE Tibet, the rigid block

415   extrusion model and the lower crustal flow model, both are able to explain parts of the

416   history of regional tectonic evolution, together with geophysical observations. The

417   rigid block extrusion model emphasizes localized strike-slip deformation along active

418   faults and oblique convergence at the plateau margin, while the lower crustal flow

419   model suggests more continuous deformation driven by viscous lower crustal flow.

420   From our perspective, since the deformation in the upper crust is unarguably

421   dominated by faults, the key point of the debate is, whether deformation of the lower

422   crust is dominated by localized shear zones or by regionally distributed lower crustal

423   flow. Since the LVZs and faulted shear zones can be observed by seismological and

424   magnetotelluric tomography, accompanied by the GPS modeling in this study (section

425   3.1; Figure 6), we argue that the rigid block extrusion model and lower crustal flow

426   model may be both required for SE Tibet.

4.1.1. Geodynamic implications: faults and LVZs

428   First, our interpretation is supported by several observations from the strain rate

429   maps and tectonics. One proof is the NE-trending "tail" (Figure 9c) in the Simao

430   Terrane, which might be the result of left-lateral shear deformation of the LVZ at

431   depth extending from the Xiaojiang fault across the Red River fault. This indicates

432   that deformation occurs in the mid-lower crust where no NE-trending faults have

433   developed, and a similar example is the "tail" extending from the Lijiang-Xiaojinhe

434   fault at Baoshan. Second, our arguments are supported by the low slip rate and

435   inactive seismicity at the Red River fault, but the higher slip rate and greater

436   seismicity at the parallel Chuxiong fault (Figure 4b and 8d). This is probably because

437   the connection between the two LVZs is localized beneath the Chuxiong fault (Figure

438   5a and 5b), and because the right-lateral shear rate shifts from the Red River fault to

439   the adjacent Chuxiong fault.

440   At a larger scale, two localized channel flows cause rapid southwestward motion:

441   one is from Songpan-Ganzi Terrane, along the Lijiang-Xiaojinhe fault to Baoshan city;

442   and the other is from the Xiaojiang fault to the Simao Terrane (Figure 6b and 9c). The

443   existence of these two channel flows is also verified by the southwestern bulge of the

444   Lancang River at Baoshan (Socquet & Pubellier, 2005) and the Red River,

445   Babianjiang and Wuliangshan faults in the Simao Terrane (Schoenbohm et al., 2006).

446   Due to these two LVZs branch from the arcuate Xianshuihe-Xiaojiang-Dien Bien Phu

447   fault, the slip rate of these three faults decreases from north to south (~15, 10, 3

448   mm/yr). In addition, the direction of flow motion is largely determined by the

449   structure of the LVZs, since they are isolated by the bounding strong terranes. Due to

450   the very limited connection between the two LVZs and the terminus of the LVZ at the

451   boundary of the South China and Chuandian Blocks, the crustal flow migrates to the

452   southwest but not to the southeast.

453   **4.1.2. The bookshelf model**

454   The well-known bookshelf model in the Shan-Thai Plateau was previously

455   described as a series of rotating parallel rectangular blocks confined by two right-

456   lateral strike slip faults (the Red River and Sagaing faults) (Leloup et al., 1995;

457   Lacassin et al., 1997, 1998; Tapponnier et al., 2001). However, this model cannot

458   explain the absence of obvious northward motion of the blocks driven by the large

459   slip rate of the Sagaing fault (~18 mm/yr; Maurin et al., 2010) and rather slow slip

460   rate of the Red River fault (~1-2 mm/yr; Shen et al., 2005) (Figure 3a). Therefore, the

461   left-lateral strike-slip faults in the bookshelf model may be driven by the paralleling

462   shear from the northwestern LVZ on the northern margin (Tengchong).

463   The actual tectonic map may be more complex than the model. At the

464   northeastern side of the Lancang-Mengzhe fault in the Simao Terrane, there are

465   several NW-trending right-lateral faults, but few NE-trending, left-lateral faults

466   (Figure 1b). This can be explained by localized deformation in the underlying LVZ

467   (discussed in the section 4.1.1), which may transfer the localized left-lateral

468   deformation along the Xiaojiang fault southwestward to the more distributed faults

469   (Figure 9c and 9d).

470   **4.2. Revision on crustal flow: rheology and partial melting**

471   The lower crustal layer in the crustal flow model is typically regarded as a

472   widespread weak sheet in the jelly sandwich model. However, Jackson (2002) argued

473   that the presence of the weak crustal layer can only be ascribed to additional partial

474   melt or fluid. In addition, small-scale low anomalies in the seismic tomography of

475   Tibetan crust are often thought to be the result of this type of chemical anomaly

476   (Hacker et al., 2014). Therefore, an alternative means can be used to define the lower

477   crustal flow: as the localized LVZs constrained by seismic tomography. In this

478   approach, the crustal flow is at a much shallower depth of the middle crust (~10-40

479   km) and does not reach the Moho discontinuity. The absence of LVZs beneath the

480   Sichuan Basin and Panzhihua-Xichang (Figure 5) may account for the large

481   topographic relief at their northwestern periphery (Figure 1a; Clark et al., 2005).

482   Therefore the localized LVZs blocked by the surrounding strong terranes may not

483   flow as was once believed (Clark & Royden, 2000). They may be only able to migrate

484   with the assistance of the relative motions of the blocks and the deformation in the

485   faulted shear zones.

486   The viscosity of the mid-lower crustal flow is an important parameter that

487   determines how the entire lithosphere deforms in response to gravitational loading

488   and tectonic forces. Our estimation of viscosity (~10^{20}-10^{21} Pa·s; section 3.2; Figure

489   7c) suggested that LVZs may not be as weak as researchers once thought (Figure 10a;

490   ~10^{18} Pa·s, Clark & Royden, 2000). However, there are significant differences

491   between the results obtained by different geodynamic models (Figure 10a; Clark &

492   Royden, 2000; Flesch et al., 2001; Jiménez-Munt & Platt, 2006; Zhang et al., 2009;

493   Shao et al., 2011; Yin & Taylor, 2011; Zhu & Zhang, 2013; Huang et al., 2014; Xu et

494   al., 2014; Shi et al., 2015; Xu et al., 2016; Diao et al., 2018; Bischoff & Flesch, 2018;

495   Panda et al., 2019; Wang et al., 2019). It is worth noting that, the models may give

496   larger values for viscosity with a smaller strain rate (larger timescale), from post-

497   seismic (decades), lake-shoreline rebound (thousands of years), to geodynamics

498   (millions of years). Therefore, it suggests that mid-lower crust could be regarded as

499   non-Newtonian fluid, and the deformation of that may be dominated by dislocation

500   creep. This rate-dependent rheology may be the major reason for the differences of

501   viscosity estimations.

502   In order to know the current status of LVZs, we evaluated whether partial melting

503   is required to explain the estimated viscosity in this study. First, the temperature

504   profiles for the crust of the Sichuan Basin, Panzhihua-Xichang, Dali (northwestern

505   LVZ), and Kunming (southeastern LVZ) were calculated as a two-layer model

506   constrained by two sets of data, heat flow and thermal conductivity from the

507   International Heat Flow Commission (IHFC; http://www.ihfc-

508   iugg.org/products/global-heat-flow-database; Wang & Huang, 1987; Hu et al., 2000;

509   Wang, 2001), and were constrained by the depth of the Curie surface as well (Figure

510   10b; Hemant & Mitchell, 2009; Gao et al., 2015). As seen in Figure 10b, the

511   temperature for dehydration melting is reached for the middle crust of LVZs.

512   Second, the viscosity profiles for wet quartzite, wet feldspar and partially molten

513   wet granite were illustrated in Figure 10c according to the temperature profiles of two

514   LVZs (Hirth et al., 2001; Rutter & Brodie, 2004; Rutter et al., 2006; Rybacki et al.,

515   2006; Bürgmann & Dresen, 2008). Thus the viscosity of the mid-lower crust beneath

516   wet solidus is too low to be explained by structural water and is likely to be partially

517   molten.

518   In addition, partial melting is needed to explain the low electrical resistivity of the

519   LVZs (~3-10 $\Omega \cdot m$; Bai et al., 2010; Rippe & Unsworth, 2010; Zhao et al., 2012;

520   Dong et al., 2016; Cheng et al., 2019; Li et al., 2019a; Xue et al., 2019; Zhao et al.,

521   2019), based on the measurements of hydrous peraluminous granitic melt (Guo et al.,

522   2018). The high Poisson's ratio of the LVZs (Li et al., 2017a; Deng et al., 2018; Tao

523   et al., 2018) indicates partial melting as well (Takei, 2002; Brantut & David, 2018). In

524   conclusion, the LVZs in the mid-lower crust are partially molten, which possibly

525   results from both the high temperature and dehydration of hydrous minerals.

526   **5. Conclusions**

527   We presented a 3D geodynamic model of Chuandian region to reproduce the

528   instantaneous horizontal surface velocity driven by tectonic forces and topographic

529   gravitational energy. The detailed GPS velocity pattern may represent a joint

530   contribution from both faulted shear zones and two localized LVZs. This result may

531   indicate that the block extrusion model and lower crustal flow model are not mutually

532   exclusive and both required for explaining the SE Tibetan tectonics. We provided

533   additional constraints on the size and viscosity of tomography-based LVZs. These

534   results suggest that weak LVZs are bounded by surrounding strong terranes, flow

535   southwestward and possibly contribute to the clockwise movement of upper crust.

536   The strain rate maps from the best-fit model could give some clues into complex

537   deformation of strike-slip faults and extensional basins in SE Tibet. In addition, the

538   estimation of the viscosity of LVZs (10^{20}-10^{21} Pa·s) suggests that rocks are probably

539   partially molten, due to the high temperature and dehydration.

References

Audet, P., & Bürgmann, R. (2011). Dominant role of tectonic inheritance in supercontinent cycles. *Nature Geoscience*, 4(3), 184. https://doi.org/10.1038/ngeo1080

Avouac, J. P., & Tapponnier, P. (1993). Kinematic model of active deformation in central Asia. *Geophysical Research Letters*, 20(10), 895-898. https://doi.org/10.1029/93GL00128

Bai, D., Unsworth, M. J., Meju, M. A., Ma, X., Teng, J., Kong, X., ... & Zhao, C. (2010). Crustal deformation of the eastern Tibetan plateau revealed by magnetotelluric imaging. *Nature geoscience*, 3(5), 358-362. https://doi.org/10.1038/ngeo830

Bao, X., Sun, X., Xu, M., Eaton, D. W., Song, X., Wang, L., ... & Huang, Z. (2015). Two crustal low-velocity channels beneath SE Tibet revealed by joint inversion of Rayleigh wave dispersion and receiver functions. *Earth and Planetary Science Letters*, 415, 16-24. https://doi.org/10.1016/j.epsl.2015.01.020

Becker, T. W., & Faccenna, C. (2011). Mantle conveyor beneath the Tethyan collisional belt. *Earth and Planetary Science Letters*, 310(3–4), 453–461. https://doi.org/10.1016/j.epsl.2011.08.021

Bendick, R., & Flesch, L. (2013). A review of heterogeneous materials and their implications for relationships between kinematics and dynamics in continents. *Tectonics*, 32(4), 980-992. https://doi.org/10.1002/tect.20058

Bischoff, S. H., & Flesch, L. M. (2018). Normal faulting and viscous buckling in the Tibetan Plateau induced by a weak lower crust. *Nature communications*, 9(1), 4952. https://doi.org/10.1038/s41467-018-07312-9

Bischoff, S., & Flesch, L. (2019). Impact of Lithospheric Strength Distribution on India-Eurasia Deformation From 3-D Geodynamic Models. *Journal of Geophysical Research: Solid Earth*, 124(1), 1084-1105. https://doi.org/10.1029/2018JB015704

Brantut, N., & David, E. C. (2018). Influence of fluids on VP/VS ratio: increase or decrease?. *Geophysical Journal International*, 216(3), 2037-2043. https://doi.org/10.1093/gji/ggy518

Burchfiel, B. C., Royden, L. H., van der Hilst, R. D., Hager, B. H., Chen, Z., King, R. W., et al. (2008). A geological and geophysical context for the Wenchuan earthquake of 12 May 2008, Sichuan, People's Republic of China. *GSA Today*, 18(7), 4– 10. doi: 10.1130/GSATG18A.1

Bürgmann, R., & Dresen, G. (2008). Rheology of the lower crust and upper mantle: Evidence from rock mechanics, geodesy, and field observations. *Annu. Rev. Earth Planet. Sci.*, 36, 531-567. https://doi.org/10.1146/annurev.earth.36.031207.124326

Carpenter, B. M., Marone, C., & Saffer, D. M. (2011). Weakness of the San Andreas Fault revealed by samples from the active fault zone. *Nature Geoscience*, 4(4), 251. https://doi.org/10.1038/ngeo1089

Chen, L., Capitanio, F. A., Liu, L., & Gerya, T. V. (2017a). Crustal rheology controls on the Tibetan plateau formation during India-Asia convergence. *Nature communications*, 8, 15992. https://doi.org/10.1038/ncomms15992

Chen, L., & Gerya, T. V. (2016). The role of lateral lithospheric strength heterogeneities in orogenic plateau growth: Insights from 3-D thermo-mechanical modeling. *Journal of Geophysical Research: Solid Earth*, 121(4), 3118-3138. https://doi.org/10.1002/2016JB012872

Chen, L., Zhan, Z., & Li, Y. (2016, January). 3D Numerical Modeling on the Present Tectonic Deformation Field in Tibetan Plateau. In *ISRM International Symposium on In-Situ Rock Stress*. International Society for Rock Mechanics and Rock Engineering.

Chen, M., Huang, H., Yao, H., van der Hilst, R., & Niu, F. (2014). Low wave speed zones in the crust beneath SE Tibet revealed by ambient noise adjoint tomography. *Geophysical Research Letters*, 41(2), 334-340. https://doi.org/10.1002/2013GL058476

Chen, M., Niu, F., Tromp, J., Lenardic, A., Lee, C. T. A., Cao, W., & Ribeiro, J. (2017b). Lithospheric foundering and underthrusting imaged beneath Tibet.

617   *Nature communications*, 8, 15659. https://doi.org/10.1038/ncomms15659

618   Chen, Y., & Wu, F. T. (1989). Lancang-Gengma earthquake: A preliminary report on
619   the November 6, 1988, event and its aftershocks. *Eos, Transactions American*
620   *Geophysical Union*, 70(49), 1527–1540. https://doi.org/10.1029/89EO00376

621   Chen, Y., Xu, Y., Xu, T., Si, S., Liang, X., Tian, X., ... & Lan, H. (2015). Magmatic
622   underplating and crustal growth in the Emeishan Large Igneous Province, SW
623   China, revealed by a passive seismic experiment. *Earth and Planetary Science*
624   *Letters*, 432, 103-114. https://doi.org/10.1016/j.epsl.2015.09.048

625   Chen, Y., Zhang, Z., Sun, C., & Badal, J. (2013). Crustal anisotropy from Moho
626   converted Ps wave splitting analysis and geodynamic implications beneath the
627   eastern margin of Tibet and surrounding regions. *Gondwana Research*, 24(3-4),
628   946-957. https://doi.org/10.1016/j.gr.2012.04.003

629   Cheng, Y., Tang, J., Chen, X., Dong, Z., & Wang, L. (2019). Crustal structure and
630   magma plumbing system beneath the Puer Basin, southwest China: Insights from
631   three-dimensional magnetotelluric imaging. *Tectonophysics*, 763, 30-45.
632   https://doi.org/10.1016/j.tecto.2019.04.032

633   Chevalier, M. L., Leloup, P. H., Replumaz, A., Pan, J., Liu, D., Li, H., ... & Métois, M.
634   (2016). Tectonic-geomorphology of the Litang fault system, SE Tibetan Plateau,
635   and implication for regional seismic hazard. *Tectonophysics*, 682, 278-292.
636   https://doi.org/10.1016/j.tecto.2016.05.039

637   Clark, M. K., Bush, J. W., & Royden, L. H. (2005). Dynamic topography produced by
638   lower crustal flow against rheological strength heterogeneities bordering the
639   Tibetan Plateau. *Geophysical Journal International*, 162(2), 575-590.
640   https://doi.org/10.1111/j.1365-246X.2005.02580.x

641   Clark, M. K., & Royden, L. H. (2000). Topographic ooze: Building the eastern
642   margin of Tibet by lower crustal flow. *Geology*, 28(8), 703-706.
643   https://doi.org/10.1130/0091-7613(2000)28<703:TOBTEM>2.0.CO;2

644   Collettini, C., Niemeijer, A., Viti, C., & Marone, C. (2009). Fault zone fabric and
645   fault weakness. *Nature*, 462(7275), 907. https://doi.org/10.1038/nature08585

646   Cook, K. L., & Royden, L. H. (2008). The role of crustal strength variations in
647   shaping orogenic plateaus, with application to Tibet. *Journal of Geophysical*
648   *Research: Solid Earth*, 113(B8). https://doi.org/10.1029/2007JB005457

649   Deng, Q., Zhang, P., Ran, Y., Yang, X., Min, W., & Chu, Q. (2003). Basic
650   characteristics of active tectonics of China. *Science in China Series D: Earth*
651   *Sciences*, 46(4), 356-372. https://xs.scihub.ltd/https://doi.org/10.1360/03yd9032

652   Deng, Y., Li, J., Song, X., & Zhu, L. (2018). Joint inversion for lithospheric structures:
653   Implications for the growth and deformation in Northeastern Tibetan Plateau.
654   *Geophysical Research Letters*, 45(9), 3951-3958.
655   https://doi.org/10.1029/2018GL077486

656   Diao, F., Wang, R., Wang, Y., Xiong, X., & Walter, T. R. (2018). Fault behavior and
657   lower crustal rheology inferred from the first seven years of postseismic GPS
658   data after the 2008 Wenchuan earthquake. *Earth and Planetary Science Letters*,
659   495, 202-212. https://doi.org/10.1016/j.epsl.2018.05.020

660   Dong, H., Wei, W., Jin, S., Ye, G., Zhang, L., Yin, Y., ... & Jones, A. G. (2016).

Extensional extrusion: Insights into south-eastward expansion of Tibetan Plateau from magnetotelluric array data. *Earth and Planetary Science Letters*, 454, 78-85. https://doi.org/10.1016/j.epsl.2016.07.043

Ekström, G., Nettles, M., & Dziewoński, A. M. (2012). The global CMT project 2004–2010: Centroid-moment tensors for 13,017 earthquakes. Physics of the *Earth and Planetary Interiors*, 200, 1-9. https://doi.org/10.1016/j.pepi.2012.04.002

England, P., & Molnar, P. (1990). Right-lateral shear and rotation as the explanation for strike-slip faulting in eastern Tibet. *Nature*, 344(6262), 140. https://doi.org/10.1038/344140a0

Flesch, L., Bendick, R., & Bischoff, S. (2018). Limitations on inferring 3D architecture and dynamics from surface velocities in the India-Eurasia collision zone. *Geophysical Research Letters*, 45(3), 1379-1386. https://doi.org/10.1002/2017GL076503

Flesch, L. M., Haines, A. J., & Holt, W. E. (2001). Dynamics of the India-Eurasia collision zone. *Journal of Geophysical Research: Solid Earth*, 106(B8), 16435-16460. https://doi.org/10.1029/2001JB000208

Gan, W., Zhang, P., Shen, Z. K., Niu, Z., Wang, M., Wan, Y., ... & Cheng, J. (2007). Present-day crustal motion within the Tibetan Plateau inferred from GPS measurements. *Journal of Geophysical Research: Solid Earth*, 112(B8). https://doi.org/10.1029/2005JB004120

Gao, G., Kang, G., Bai, C., & Wen, L. (2015). Study on crustal magnetic anomalies and Curie surface in Southeast Tibet. *Journal of Asian Earth Sciences*, 97, 169-177. https://doi.org/10.1016/j.jseaes.2014.10.035

Gao, X., & Wang, K. (2014). Strength of stick-slip and creeping subduction megathrusts from heat flow observations. *Science*, 345(6200), 1038-1041. doi: 10.1126/science.1255487

Guo, X., Zhang, L., Su, X., Mao, Z., Gao, X. Y., Yang, X., & Ni, H. (2018). Melting Inside the Tibetan Crust? Constraint From Electrical Conductivity of Peraluminous Granitic Melt. *Geophysical Research Letters*, 45(9), 3906-3913. https://doi.org/10.1029/2018GL077804

Hacker, B. R., Ritzwoller, M. H., & Xie, J. (2014). Partially melted, mica-bearing crust in Central Tibet. *Tectonics*, 33(7), 1408-1424. https://doi.org/10.1002/2014TC003545

Hemant, K., & Mitchell, A. (2009). Magnetic field modelling and interpretation of the Himalayan–Tibetan Plateau and adjoining north Indian Plains. *Tectonophysics*, 478(1-2), 87-99. https://doi.org/10.1016/j.tecto.2009.06.009

Hearn, E. H., Bürgmann, R., & Reilinger, R. E. (2002). Dynamics of Izmit earthquake postseismic deformation and loading of the Duzce earthquake hypocenter. *Bulletin of the Seismological Society of America*, 92(1), 172-193. https://doi.org/10.1785/0120000832

Hearn, E. H., McClusky, S., Ergintav, S., & Reilinger, R. E. (2009). Izmit earthquake postseismic deformation and dynamics of the North Anatolian Fault Zone. *Journal of Geophysical Research: Solid Earth*, 114(B8).

705   https://doi.org/10.1029/2008JB006026

706 Hirth, G., Teyssier, C., & Dunlap, J. W. (2001). An evaluation of quartzite flow laws
707   based on comparisons between experimentally and naturally deformed rocks.
708   *International Journal of Earth Sciences*, 90(1), 77-87.
709   https://doi.org/10.1007/s005310000152

710 Hu, S., He, L., & Wang, J. (2000). Heat flow in the continental area of China: a new
711   data set. *Earth and Planetary Science Letters*, 179(2), 407-419.
712   https://doi.org/10.1016/S0012-821X(00)00126-6

713 Huang, M. H., Bürgmann, R., & Freed, A. M. (2014). Probing the lithospheric
714   rheology across the eastern margin of the Tibetan Plateau. *Earth and Planetary*
715   *Science Letters*, 396, 88-96. https://doi.org/10.1016/j.epsl.2014.04.003

716 Huang, Z., Wang, L., Xu, M., Ding, Z., Wu, Y., Wang, P., et al. (2015). Teleseismic
717   shear-wave splitting in SE Tibet: Insight into complex crust and upper-mantle
718   deformation. *Earth and Planetary Science Letters*, 432, 354–362.
719   https://doi.org/10.1016/j.epsl.2015.10.027

720 Huang, Z., Wang, L., Xu, M., & Zhao, D. (2018). P Wave Anisotropic Tomography
721   of the SE Tibetan Plateau: Evidence for the Crustal and Upper-Mantle
722   Deformations. *Journal of Geophysical Research: Solid Earth*, 123(10), 8957-
723   8978. https://doi.org/10.1029/2018JB016048

724 Jackson, J. A. (2002). Strength of the continental lithosphere: time to abandon the
725   jelly sandwich?. *GSA today*, 12, 4-10.

726 Jiménez-Munt, I., & Platt, J. P. (2006). Influence of mantle dynamics on the
727   topographic evolution of the Tibetan Plateau: Results from numerical modeling.
728   *Tectonics*, 25(6). https://doi.org/10.1029/2006TC001963

729 Johnson, K. M., & Segall, P. (2004). Viscoelastic earthquake cycle models with deep
730   stress-driven creep along the San Andreas fault system. *Journal of Geophysical*
731   *Research: Solid Earth*, 109(B10). https://doi.org/10.1029/2004JB003096

732 Karato, S. I. (2010). Rheology of the Earth's mantle: A historical review. *Gondwana*
733   *Research*, 18(1), 17-45. https://doi.org/10.1016/j.gr.2010.03.004

734 Karato, S. I., & Wu, P. (1993). Rheology of the upper mantle: A synthesis. *Science*,
735   260(5109), 771-778. doi: 10.1126/science.260.5109.771

736 Kohlstedt, D. L., Evans, B., & Mackwell, S. J. (1995). Strength of the lithosphere:
737   Constraints imposed by laboratory experiments. *Journal of Geophysical*
738   *Research: Solid Earth*, 100(B9), 17587-17602.
739   https://doi.org/10.1029/95JB01460

740 Kreemer, C., Blewitt, G., & Klein, E. C. (2014). A geodetic plate motion and global
741   strain rate model. *Geochemistry, Geophysics, Geosystems*, 15(10), 3849-3889.
742   https://doi.org/10.1002/2014GC005407

743 Lacassin, R., Maluski, H., Leloup, P. H., Tapponnier, P., Hinthong, C., Siribhakdi, K.,
744   et al. (1997). Tertiary diachronic extrusion and deformation of western Indochina:
745   Structural and 40Ar/39Ar evidence from NW Thailand. *Journal of Geophysical*
746   *Research*, 102(B5), 10,013–10,037. https://doi.org/10.1029/96JB03831

747 Lacassin, R., Replumaz, A., & Hervé Leloup, P. (1998). Hairpin river loops and slip-
748   sense inversion on southeast Asian strike-slip faults. *Geology*, 26(8), 703–706.

749   https://doi.org/10.1130/0091-7613(1998)026<0703:HRLASS>2.3.CO;2

750   Landau, L., and E. Lifshitz (1986), Theory of Elasticity, Butterworth Heinemann,
751   Oxford, U. K

752   Leloup, P. H., Lacassin, R., Tapponnier, P., Schärer, U., Zhong, D., Liu, X., ... &
753   Trinh, P. T. (1995). The Ailao Shan-Red River shear zone (Yunnan, China),
754   Tertiary transform boundary of Indochina. *Tectonophysics*, 251(1-4), 3-84.
755   https://doi.org/10.1016/0040-1951(95)00070-4

756   Leng, W., & Gurnis, M. (2011). Dynamics of subduction initiation with different
757   evolutionary pathways. *Geochemistry, Geophysics, Geosystems*, 12(12).
758   https://doi.org/10.1029/2011GC003877

759   Leng, W., & Gurnis, M. (2015). Subduction initiation at relic arcs. *Geophysical*
760   *Research Letters*, 42(17), 7014-7021. https://doi.org/10.1002/2015GL064985

761   Lockner, D. A., Morrow, C., Moore, D., & Hickman, S. (2011). Low strength of deep
762   San Andreas fault gouge from SAFOD core. *Nature*, 472(7341), 82.
763   https://doi.org/10.1038/nature09927

764   Li, J., Song, X., Zhu, L., & Deng, Y. (2017a). Joint inversion of surface wave
765   dispersions and receiver functions with P velocity constraints: Application to
766   Southeastern Tibet. *Journal of Geophysical Research: Solid Earth*, 122(9), 7291-
767   7310. https://doi.org/10.1002/2017JB014135

768   Li, X., Bai, D., Ma, X., Chen, Y., Varentsov, I. M., Xue, G., ... & Lozovsky, I.
769   (2019a). Electrical resistivity structure of the Xiaojiang strike-slip fault system
770   (SW China) and its tectonic implications. *Journal of Asian Earth Sciences*, 176,
771   57-67. https://doi.org/10.1016/j.jseaes.2019.01.031

772   Li, Y., Chen, L., Tan, P., & Li, H. (2014). Lower crustal flow and its relation to the
773   surface deformation and stress distribution in western Sichuan region, China.
774   *Journal of Earth Science*, 25(4), 630-637. https://doi.org/10.1007/s12583-014-
775   0467-x

776   Li, Y., Jia, D., Shaw, J. H., Hubbard, J., Lin, A., Wang, M., ... & Wu, L. (2010).
777   Structural interpretation of the coseismic faults of the Wenchuan earthquake:
778   Three-dimensional modeling of the Longmen Shan fold-and-thrust belt. *Journal*
779   *of Geophysical Research: Solid Earth*, 115(B4).
780   https://doi.org/10.1029/2009JB006824

781   Li, Y., Liu, M., Li, Y., & Chen, L. (2019b). Active crustal deformation in
782   southeastern Tibetan Plateau: The kinematics and dynamics. *Earth and*
783   *Planetary Science Letters*, 523, 115708.
784   https://doi.org/10.1016/j.epsl.2019.07.010

785   Li, Y., Liu, S., Chen, L., Du, Y., Li, H., & Liu, D. (2017b). Mechanism of crustal
786   deformation in the Sichuan-Yunnan region, southeastern Tibetan Plateau:
787   Insights from numerical modeling. *Journal of Asian Earth Sciences*, 146, 142-
788   151. https://doi.org/10.1016/j.jseaes.2017.05.018

789   Liang, S., Gan, W., Shen, C., Xiao, G., Liu, J., Chen, W., ... & Zhou, D. (2013).
790   Three-dimensional velocity field of present-day crustal motion of the Tibetan
791   Plateau derived from GPS measurements. *Journal of Geophysical Research:*
792   *Solid Earth*, 118(10), 5722-5732. https://doi.org/10.1002/2013JB010503

Liu-Zeng, J., Tapponnier, P., Gaudemer, Y., & Ding, L. (2008). Quantifying landscape differences across the Tibetan plateau: Implications for topographic relief evolution. *Journal of Geophysical Research: Earth Surface*, 113(F4). https://doi.org/10.1029/2007JF000897

Luo, G., & Liu, M. (2018). Stressing Rates and Seismicity on the Major Faults in Eastern Tibetan Plateau. *Journal of Geophysical Research: Solid Earth*, 123(12), 10-968. https://doi.org/10.1029/2018JB015532

Magni, V., Faccenna, C., van Hunen, J., & Funiciello, F. (2014). How collision triggers backarc extension: Insight into Mediterranean style of extension from 3-D numerical models. *Geology*, 42(6), 511-514. https://doi.org/10.1130/G35446.1

Maurin, T., Masson, F., Rangin, C., Min, U. T., & Collard, P. (2010). First global positioning system results in northern Myanmar: Constant and localized slip rate along the Sagaing fault. *Geology*, 38(7), 591-594. https://doi.org/10.1130/G30872.1

Meade, B. J., & Loveless, J. P. (2009). Block modeling with connected fault-network geometries and a linear elastic coupling estimator in spherical coordinates. *Bulletin of the Seismological Society of America*, 99(6), 3124-3139. https://doi.org/10.1785/0120090088

Moresi, L., Zhong, S., & Gurnis, M. (1996). The accuracy of finite element solutions of Stokes's flow with strongly varying viscosity. *Physics of the Earth and Planetary Interiors*, 97(1-4), 83-94. https://doi.org/10.1016/0031-9201(96)03163-9

Moresi, L., Dufour, F., & Mühlhaus, H. B. (2003). A Lagrangian integration point finite element method for large deformation modeling of viscoelastic geomaterials. *Journal of computational physics*, 184(2), 476-497. https://doi.org/10.1016/S0021-9991(02)00031-1

Niemeijer, A., Marone, C., & Elsworth, D. (2010). Frictional strength and strain weakening in simulated fault gouge: Competition between geometrical weakening and chemical strengthening. *Journal of Geophysical Research: Solid Earth*, 115(B10). https://doi.org/10.1029/2009JB000838

Okada, Y. (1985). Surface deformation due to shear and tensile faults in a half-space. *Bulletin of the seismological society of America*, 75(4), 1135-1154.

Pan, G., Wang, L., & Zhu, D. (2004). Thoughts on some important scientific problems in regional geological survey of the Qinghai-Tibet Plateau [J]. *Regional Geology of China*, 1, 12-19.

Panda, D., Kundu, B., & Santosh, M. (2018). Oblique convergence and strain partitioning in the outer deformation front of NE Himalaya. *Scientific reports*, 8(1), 10564. https://doi.org/10.1038/s41598-018-28774-3

Panda, D., Mondal, A., & Kundu, B. (2019). Eastward "glacier-like flow" of the Tibetan crust constrained from power-law rheology. *Journal of Asian Earth Sciences*, 177, 129-133. https://doi.org/10.1016/j.jseaes.2019.03.021

Pasyanos, M. E., Masters, T. G., Laske, G., & Ma, Z. (2014). LITHO1. 0: An updated crust and lithospheric model of the Earth. *Journal of Geophysical Research: Solid Earth*, 119(3), 2153-2173. https://doi.org/10.1002/2013JB010626

Peltzer, G., & Tapponnier, P. (1988). Formation and evolution of strike-slip faults, rifts, and basins during the India-Asia collision: An experimental approach. Journal of Geophysical Research: Solid Earth, 93(B12), 15085-15117.

Poliakov, A. N., & Buck, W. R. (1998). Mechanics of stretching elastic-plastic-viscous layers: Applications to slow-spreading mid-ocean ridges. *Geophysical Monograph-American Geophysical Union*, 106, 305-324.

Ren, J., Xu, X., Yeats, R. S., & Zhang, S. (2013). Latest Quaternary paleoseismology and slip rates of the Longriba fault zone, eastern Tibet: Implications for fault behavior and strain partitioning. *Tectonics*, 32(2), 216-238. https://doi.org/10.1002/tect.20029

Rippe, D., & Unsworth, M. (2010). Quantifying crustal flow in Tibet with magnetotelluric data. *Physics of the Earth and Planetary Interiors*, 179(3-4), 107-121. https://doi.org/10.1016/j.pepi.2010.01.009

Royden, L. H., Burchfiel, B. C., King, R. W., Wang, E., Chen, Z., Shen, F., & Liu, Y. (1997). Surface deformation and lower crustal flow in eastern Tibet. *science*, 276(5313), 788-790. doi: 10.1126/science.276.5313.788

Royden, L. H., Burchfiel, B. C., & van der Hilst, R. D. (2008). The geological evolution of the Tibetan Plateau. *science*, 321(5892), 1054-1058. doi: 10.1126/science.1155371

Rutter, E. H., & Brodie, K. H. (2004). Experimental grain size-sensitive flow of hot-pressed Brazilian quartz aggregates. *Journal of Structural Geology*, 26(11), 2011-2023. https://doi.org/10.1016/j.jsg.2004.04.006

Rutter, E. H., Brodie, K. H., & Irving, D. H. (2006). Flow of synthetic, wet, partially molten "granite" under undrained conditions: an experimental study. *Journal of Geophysical Research: Solid Earth*, 111(B6). https://doi.org/10.1029/2005JB004257

Rybacki, E., Gottschalk, M., Wirth, R., & Dresen, G. (2006). Influence of water fugacity and activation volume on the flow properties of fine-grained anorthite aggregates. *Journal of Geophysical Research: Solid Earth*, 111(B3). https://doi.org/10.1029/2005JB003663

Savage, J. C., & Burford, R. O. (1973). Geodetic determination of relative plate motion in central California. *Journal of Geophysical Research*, 78(5), 832-845. https://doi.org/10.1029/JB078i005p00832

Schoenbohm, L. M., Burchfiel, B. C., Liangzhong, C., & Jiyun, Y. (2006). Miocene to present activity along the Red River fault, China, in the context of continental extrusion, upper-crustal rotation, and lower-crustal flow. *Geological Society of America Bulletin*, 118(5-6), 672-688. https://doi.org/10.1130/B25816.1

Shao, Z., Wang, R., Wu, Y., & Zhang, L. (2011). Rapid afterslip and short-term viscoelastic relaxation following the 2008 M W 7.9 Wenchuan earthquake. *Earthquake Science*, 24(2), 163-175. https://doi.org/10.1007/s11589-010-0781-z

Shen, W., Ritzwoller, M. H., Kang, D., Kim, Y., Lin, F. C., Ning, J., ... & Zhou, L. (2016). A seismic reference model for the crust and uppermost mantle beneath China from surface wave dispersion. *Geophysical Journal International*, 206(2), 954-979. https://doi.org/10.1093/gji/ggw175

Shen, Z. K., Lü, J., Wang, M., & Bürgmann, R. (2005). Contemporary crustal deformation around the southeast borderland of the Tibetan Plateau. *Journal of Geophysical Research: Solid Earth*, 110(B11). https://doi.org/10.1029/2004JB003421

Shi, F. (2014). Tectonic geomorphology of the Nantinghe Fault in Southwestern Yunnan. PhD thesis (in Chinese with English abstract). Institute of Geology, China Earthquake Administration Beijing.

Shi, X., Kirby, E., Furlong, K. P., Meng, K., Robinson, R., & Wang, E. (2015). Crustal strength in central Tibet determined from Holocene shoreline deflection around Siling Co. *Earth and Planetary Science Letters*, 423, 145-154. https://doi.org/10.1016/j.epsl.2015.05.002

Shi, X., Wang, Y., Sieh, K., Weldon, R., Feng, L., Chan, C. H., & Liu-Zeng, J. (2018). Fault slip and GPS velocities across the Shan Plateau define a curved southwestward crustal motion around the eastern Himalayan syntaxis. *Journal of Geophysical Research: Solid Earth*, 123(3), 2502-2518. https://doi.org/10.1002/2017JB015206

Smith-Konter, B. R., Sandwell, D. T., & Shearer, P. (2011). Locking depths estimated from geodesy and seismology along the San Andreas Fault System: Implications for seismic moment release. *Journal of Geophysical Research: Solid Earth*, 116(B6). https://doi.org/10.1029/2010JB008117

Socquet, A., & Pubellier, M. (2005). Cenozoic deformation in western Yunnan (China–Myanmar border). *Journal of Asian Earth Sciences*, 24(4), 495-515. https://doi.org/10.1016/j.jseaes.2004.03.006

Sternai, P., Avouac, J. P., Jolivet, L., Faccenna, C., Gerya, T., Becker, T. W., & Menant, A. (2016). On the influence of the asthenospheric flow on the tectonics and topography at a collision-subduction transition zones: Comparison with the eastern Tibetan margin. *Journal of Geodynamics*, 100, 184-197. https://doi.org/10.1016/j.jog.2016.02.009

Sun, X., Bao, X., Xu, M., Eaton, D. W., Song, X., Wang, L., ... & Li, H. (2014). Crustal structure beneath SE Tibet from joint analysis of receiver functions and Rayleigh wave dispersion. *Geophysical Research Letters*, 41(5), 1479-1484. https://doi.org/10.1002/2014GL059269

Tackley, P. J. (2000). Self-consistent generation of tectonic plates in time-dependent, three-dimensional mantle convection simulations 2. Strain weakening and asthenosphere. *Geochemistry, Geophysics, Geosystems*, 1(8). https://doi.org/10.1029/2000GC000043

Takei, Y. (2002). Effect of pore geometry on Vp/Vs: From equilibrium geometry to crack. *Journal of Geophysical Research: Solid Earth*, 107(B2), ECV-6. ttps://doi.org/10.1029/2001JB000522

Tao, K., Grand, S. P., & Niu, F. (2018). Seismic structure of the upper mantle beneath Eastern Asia from full waveform seismic tomography. *Geochemistry, Geophysics, Geosystems*, 19(8), 2732-2763. https://doi.org/10.1029/2018GC007460

Tapponnier, P., Peltzer, G. L. D. A. Y., Le Dain, A. Y., Armijo, R., & Cobbold, P.

(1982). Propagating extrusion tectonics in Asia: New insights from simple experiments with plasticine. *Geology*, 10(12), 611-616. https://doi.org/10.1130/0091-7613(1982)10<611:PETIAN>2.0.CO;2

Tapponnier, P., Zhiqin, X., Roger, F., Meyer, B., Arnaud, N., Wittlinger, G., & Jingsui, Y. (2001). Oblique stepwise rise and growth of the Tibet Plateau. *science*, 294(5547), 1671-1677. doi: 10.1126/science.105978

Taylor, M., & Yin, A. (2009). Active structures of the Himalayan-Tibetan orogen and their relationships to earthquake distribution, contemporary strain field, and Cenozoic volcanism. *Geosphere*, 5(3), 199-214. https://doi.org/10.1130/GES00217.1

Tunini, L., Jiménez-Munt, I., Fernandez, M., Vergés, J., & Bird, P. (2017). Neotectonic deformation in central Eurasia: A geodynamic model approach. *Journal of Geophysical Research: Solid Earth*, 122(11), 9461-9484. https://doi.org/10.1002/2017JB014487

Wang, E. (Ed.). (1998). *Late Cenozoic Xianshuihe-Xiaojiang, Red River, and Dali fault systems of southwestern Sichuan and central Yunnan, China* (Vol. 327). Geological Society of America.

Wang, J. H., Yin, A., Harrison, T. M., Grove, M., Zhang, Y. Q., & Xie, G. H. (2001). A tectonic model for Cenozoic igneous activities in the eastern Indo–Asian collision zone. *Earth and Planetary Science Letters*, 188(1-2), 123-133. https://doi.org/10.1016/S0012-821X(01)00315-6

Wang, J. Y., & Huang, S. P. (1987). Linear relationship between heat flow and heat production in Panxi Paleorift Zone, southwestern China. *Geophysical Research Letters*, 14(3), 272-274. https://doi.org/10.1029/GL014i003p00272

Wang, Q., Xu, X., Shyu, J. B. H., Jiang, Z., Liu, S., Wu, Y., ... & Wei, W. (2019). Viscoelastic behavior of the crust around the Longmenshan Thrust Belt inferred from post-seismic deformation of the 2013 Lushan earthquake, China. *Journal of Asian Earth Sciences*, 173, 386-396. https://doi.org/10.1016/j.jseaes.2019.02.001

Wang, W., Qiao, X., Yang, S., & Wang, D. (2016). Present-day velocity field and block kinematics of Tibetan Plateau from GPS measurements. *Geophysical Journal International*, 208(2), 1088-1102. https://doi.org/10.1093/gji/ggw445

Wang, W., Wu, J., Fang, L., Lai, G., Yang, T., & Cai, Y. (2014). S wave velocity structure in southwest China from surface wave tomography and receiver functions. *Journal of Geophysical Research: Solid Earth*, 119(2), 1061-1078. https://doi.org/10.1002/2013JB010317

Wang, Y. (2001). Heat flow pattern and lateral variations of lithosphere strength in China mainland: constraints on active deformation. *Physics of the Earth and Planetary Interiors*, 126(3-4), 121-146. https://doi.org/10.1016/S0031-9201(01)00251-5

Wang, Y., Zhang, X., Jiang, C., Wei, H., & Wan, J. (2007). Tectonic controls on the late Miocene–Holocene volcanic eruptions of the Tengchong volcanic field along the southeastern margin of the Tibetan plateau. *Journal of Asian Earth Sciences*, 30(2), 375-389. https://doi.org/10.1016/j.jseaes.2006.11.005

Wei, W., Zhao, D., & Xu, J. (2013). P-wave anisotropic tomography in Southeast

Tibet: New insight into the lower crustal flow and seismotectonics. *Physics of the Earth and Planetary Interiors*, 222, 47-57. https://doi.org/10.1016/j.pepi.2013.07.002

Wu, T., Zhang, S., Li, M., Qin, W., & Zhang, C. (2016). Two crustal flowing channels and volcanic magma migration underneath the SE margin of the Tibetan Plateau as revealed by surface wave tomography. *Journal of Asian Earth Sciences*, 132, 25-39. https://doi.org/10.1016/j.jseaes.2016.09.017

Wu, X., Xu, X., Yu, G., Cheng, J., Chen, G., An, Y., & W, Q. (2018). The map of surface rupture of national earthquake experiment field in Chuan-Dian. Seismology and Geology, 40(1), 27-41. (in Chinese)

Xu, C. J., Fan, Q. B., Wang, Q., Yang, S. M., & Jiang, G. Y. (2014). Postseismic deformation after 2008 wenchuan earthquake. *Survey Review*, 46(339), 432-436. https://doi.org/10.1179/1752270614Y.0000000128

Xu, X., Keller, G. R., Gao, R., Guo, X., & Zhu, X. (2016). Uplift of the Longmen Shan area in the eastern Tibetan Plateau: an integrated geophysical and geodynamic analysis. *International Geology Review*, 58(1), 14-31. https://doi.org/10.1080/00206814.2015.1055595

Xu, X., Wen, X., Han, Z., Chen, G., Li, C., Zheng, W., ... & Wei, Z. (2013). Lushan M S 7.0 earthquake: A blind reserve-fault event. *Chinese Science Bulletin*, 58(28-29), 3437-3443. https://doi.org/10.1007/s11434-013-5999-4

Xu, X., Wen, X., Yu, G., Chen, G., Klinger, Y., Hubbard, J., & Shaw, J. (2009). Coseismic reverse-and oblique-slip surface faulting generated by the 2008 Mw 7.9 Wenchuan earthquake, China. *Geology*, 37(6), 515-518. https://doi.org/10.1130/G25462A.1

Xu, X., Wen, X., Yu, G., Zheng, R., Luo, H., & Zheng, B. (2005). Average slip rate, earthquake rupturing segmentation and recurrence behavior on the Litang fault zone, western Sichuan Province, China. *Science in China Series D: Earth Sciences*, 48(8), 1183-1196. https://doi.org/10.1360/04yd0072

Xue, S., Bai, D., Chen, Y., Ma, X., Chen, L., Li, X., & Yan, Y. (2019). Contrasting crustal deformation mechanisms in the Longmenshan and West Qinling orogenic belts, NE Tibet, revealed by magnetotelluric data. *Journal of Asian Earth Sciences*, 176, 120-128. https://doi.org/10.1016/j.jseaes.2019.01.039

Yang, H., & Duan, Y. (2019). High-resolution crustal structure illuminated by ultra-dense array recordings. *Acta Geologica Sinica-English Edition*, 93, 284-284.

Yang, T., Wu, J., Fang, L., & Wang, W. (2014). Complex Structure beneath the Southeastern Tibetan Plateau from Teleseismic P-Wave Tomography. *Bulletin of the Seismological Society of America*, 104(3), 1056-1069. https://doi.org/10.1785/0120130029

Yang, Y., & Liu, M. (2009). Crustal thickening and lateral extrusion during the Indo-Asian collision: A 3D viscous flow model. *Tectonophysics*, 465(1-4), 128-135. https://doi.org/10.1016/j.tecto.2008.11.002

Yang, Y., Yao, H., Wu, H., Zhang, P., & Wang, M. (2020). A new crustal shear-velocity model in Southwest China from joint seismological inversion and its implications for regional crustal dynamics. *Geophysical Journal International*,

220(2), 1379-1393. https://doi.org/10.1093/gji/ggz514

Yao, H., Van Der Hilst, R. D., & Montagner, J. P. (2010). Heterogeneity and anisotropy of the lithosphere of SE Tibet from surface wave array tomography. *Journal of Geophysical Research: Solid Earth*, 115(B12). https://doi.org/10.1029/2009JB007142

Yin, A., & Harrison, T. M. (2000). Geologic evolution of the Himalayan-Tibetan orogen. *Annual review of earth and planetary sciences*, 28(1), 211-280. https://doi.org/10.1146/annurev.earth.28.1.211

Yin, A., & Taylor, M. H. (2011). Mechanics of V-shaped conjugate strike-slip faults and the corresponding continuum mode of continental deformation. *GSA Bulletin*, 123(9-10), 1798-1821. https://doi.org/10.1130/B30159.1

Yin, F., Jiang, C., Jia, K., Han, L., & Zhang, H. (2019). A study on seismicity in the Yunnan region by using the multidimensional stress release model. *Physics of the Earth and Planetary Interiors*, 289, 115-122. https://doi.org/10.1016/j.pepi.2019.01.007

Zhang, C., Cao, J., & Shi, Y. (2009). Studying the viscosity of lower crust of Qinghai-Tibet Plateau according to post-seismic deformation. *Science in China Series D: Earth Sciences*, 52(3), 411-419. https://doi.org/10.1007/s11430-009-0028-9

Zhang, P., Deng, Q., Zhang, G., Ma, J., Gan, W., Min, W., ... & Wang, Q. (2003). Active tectonic blocks and strong earthquakes in the continent of China. *Science in China Series D: Earth Sciences*, 46(2), 13-24. https://doi.org/10.1360/03dz0002

Zhang, S., & Liu, B. (1978). Seismic characteristicis of Tonghai earthquake in 1970 (in Chinese with English abstract). *Scientia Geologica Sinica*, (4), 323–335.

Zhao, G., Unsworth, M. J., Zhan, Y., Wang, L., Chen, X., Jones, A. G., ... & Li, T. (2012). Crustal structure and rheology of the Longmenshan and Wenchuan Mw 7.9 earthquake epicentral area from magnetotelluric data. *Geology*, 40(12), 1139-1142. https://doi.org/10.1130/G33703.1

Zhao, L. F., Xie, X. B., He, J. K., Tian, X., & Yao, Z. X. (2013). Crustal flow pattern beneath the Tibetan Plateau constrained by regional Lg-wave Q tomography. *Earth and Planetary Science Letters*, 383, 113-122. https://doi.org/10.1016/j.epsl.2013.09.038

Zhao, Y., Ye, G., Dong, J. E., Wei, W., & Jin, S. (2019). Electrical Constraints on the channel flow underneath the northeastern Tibetan plateau: Results of the Longriba-Minjiang magnetotelluric sounding profile. *Journal of Asian Earth Sciences*, 170, 73-83. https://doi.org/10.1016/j.jseaes.2018.10.004

Zheng, G., Wang, H., Wright, T. J., Lou, Y., Zhang, R., Zhang, W., ... & Wei, N. (2017). Crustal deformation in the India-Eurasia collision zone from 25 years of GPS measurements. *Journal of Geophysical Research: Solid Earth*, 122(11), 9290-9312. https://doi.org/10.1002/2017JB014465

Zhu, A., Zhang, D., & Jiang, C. (2016). Numerical simulation of the segmentation of the stress state of the Anninghe-Zemuhe-Xiaojiang faults. *Science China Earth Sciences*, 59(2), 384-396. https://doi.org/10.1007/s11430-015-5157-8

Zhu, S., & Zhang, P. (2013). FEM simulation of interseismic and coseismic

1057   deformation associated with the 2008 Wenchuan Earthquake. *Tectonophysics*,
1058   584, 64-80. https://doi.org/10.1016/j.tecto.2012.06.024
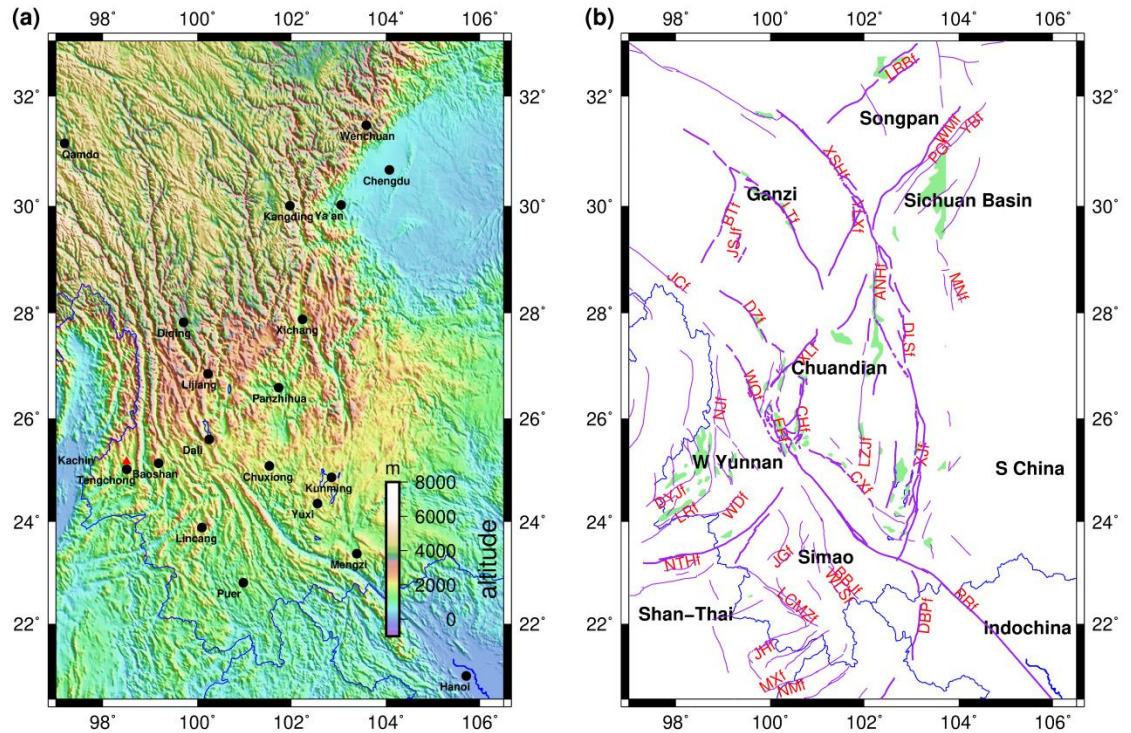
Figure 1. (**a**) Topography (ETOPO5, National Geophysical Data Center, 1993) of SE

Tibet, with the cities by the black dots and the volcano indicated by the red

triangle. (**b**) Faults and blocks in southeastern Tibet. The purple lines indicate the

map of geological fault segments (Zhang et al., 2003; Taylor & Yin, 2009; Wu et

al., 2018; Shi et al., 2018) and basins (green shading, provided by the Earth

Observation from Space Data Sub-center, http://data.cea-ies.ac.cn). The name

and Abbreviations are listed below. ANHf—Anninghe fault; BBJf—Babianjiang

fault; BTf—Batang fault; CHf—Chenghai fault; CXf—Chuxiong fault; DBPf—

Dien Bien Phu fault; DLSf—Daliangshan fault; DYJf—Dayingjiang fault;

DZf—Deqing-Zhongdian fault; EEf—Erhai-Eryuan fault; JGf—Jinggu fault;

JHf—Jinghong fault; JSJf—Jinshajiang fault; LRBf—Longriba fault; LCMZf—

1071   Lancang-Mengzhe fault; LRf—Longling-Ruili fault; LTf—Litang fault; LZJf—

1072   Lvzhijiang fault; MNf—Manao fault; MXf—Mengxing fault; NJf—Nujiang

1073   fault; NMf—Nam Ma fault; NTHf—Nantinghe fault; PGf—Pengguan fault;

1074   RRf—Red River fault; WDf—Wanding fault; WLSf—Wuliangshan fault;

1075   WMf—Wenchuan-Maowen fault; WQf—Weixi-Qiaohou fault; XJf—Xiaojiang

1076   fault; XLf—Xiaojinhe-Lijiang fault; XSHf—Xianshuihe fault; YBf—Yingxiu-

1077   Beichuan fault; YLXf—Yulongxi fault.

1078
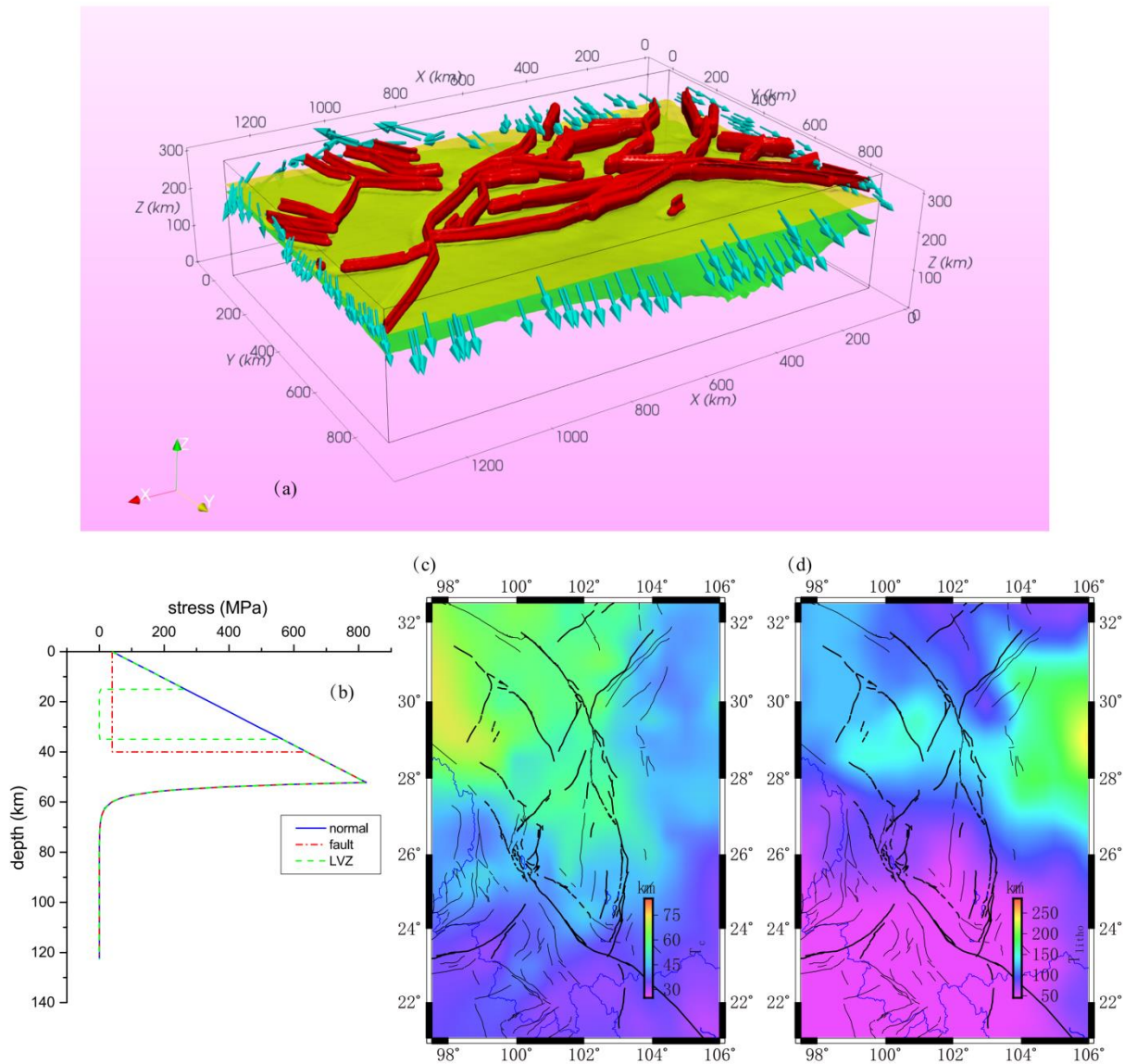
1079   **Figure 2.** (**a**) The geodynamic model of SE Tibet with faulted shear zones (red),

1080   Moho (yellow), LAB (green), and imposed velocity boundary conditions at the

1081   surrounding margin of the entire lithosphere (blue). Axis x: south; axis y: east;

1082   axis z: upwards. (**b**) Sketches of strength vs. depth. The blue solid line shows the

1083   profile for areas without faulted shear zone or an LVZ layer; the red dashed-

1084   dotted line shows the profile for areas with faulted shear zones down to the

1085   Moho; the green dashed line shows the profile for areas with an extra LVZ layer

1086   from 15 km to 35 km, with a viscosity of 10^{20} Pa·s. The Moho depth is set to be

1087   40 km; the frictional coefficient, initial cohesion of friction, μ and C_0, are set to

1088   0.5 and 40 MPa, respectively. The other parameters for rheology are listed in

1089   Table 1. For all depths, the reference strain rate is constant at 10^{-15} s^{-1}. (**c**) Moho

1090   depth, from Yang et al. (2020). (**d**) Lithosphere thickness, from Litho_1.0

1091   (Pasyanos et al., 2014).

1092
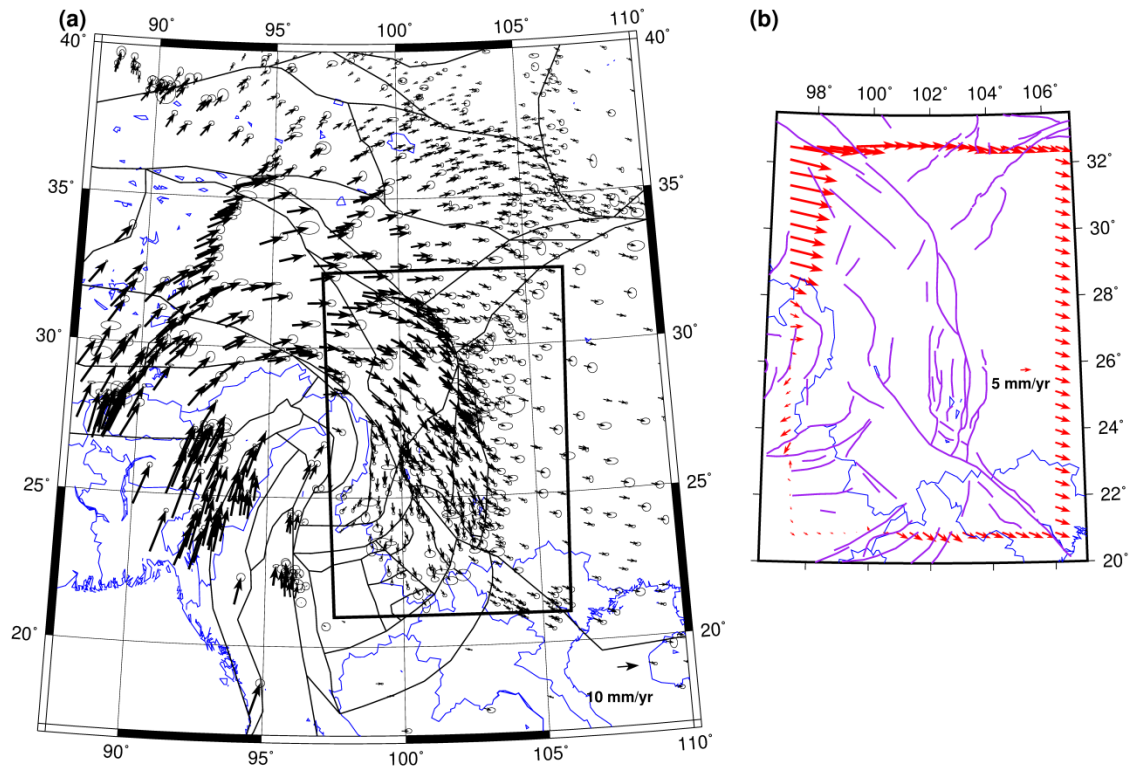
1093 **Figure 3.** (**a**) Interseismic (25 years) GPS data (black vectors), from Zheng et al.

1094 (2017), in the reference frame of stable Eurasian Plate. The black rectangle

1095 indicates the study area. (**b**) The lateral velocity boundary conditions used in the

1096 model, which are computed based on the Blocks model of Meade & Loveless

1097 (2009), in which we used a fault-block network (thin solid black lines in **a**) based

1098 on the fault traces from Taylor & Yin (2009) (purple lines in **b**).

1099
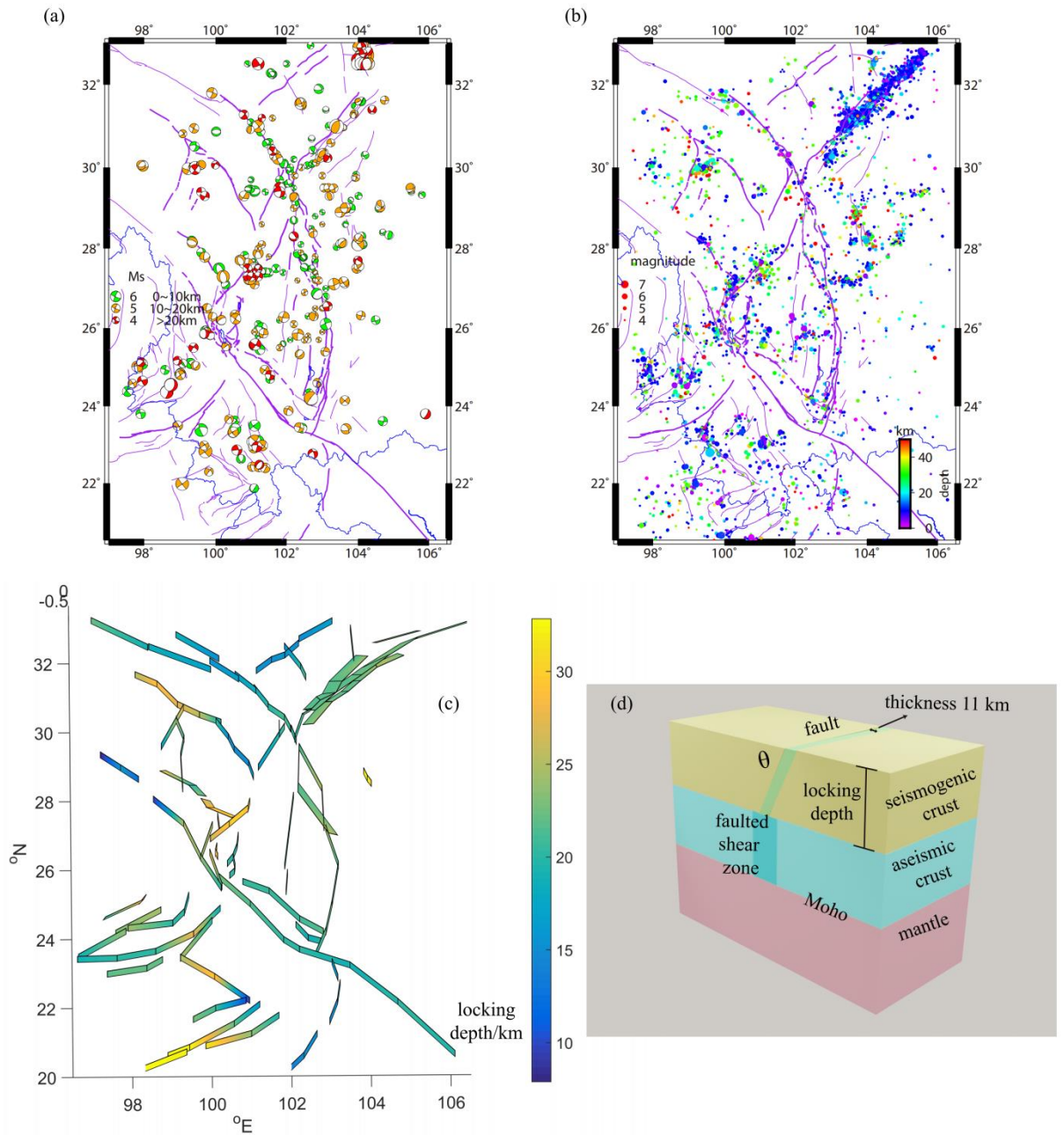
Figure 4. (**a**) Map of the focal mechanism in SE Tibet from the China Earthquake

Data Center, from 1966 to 2015, which was used to estimate the dip angle of the

adjacent faults. The magnitudes and depth ranges of earthquakes are given in the

legend. (**b**) Map of earthquake locations from IRIS (http://ds.iris.edu/wilber3/),

from 1968 to 2018, with magnitude > 4. The magnitude and depth are scaled in

the colored map and legend. (**c**) 3D fault model (upper part only) in SE Tibet

1106   used in this study, constrained by earthquake locations, focal mechanisms, and

1107   geological studies of faults, with strike, dip angle, and locking depth (scaled by

1108   the colored map). The selected faults were all active in the Holocene. (**d**) Sketch

1109   of the structure of the faulted shear zone. The upper part of faulted shear zone

1110   has a thickness of 11 km and θ represents the dip angle; a thicker faulted shear

1111   zone is shown from the locking depth to Moho depth.


1112
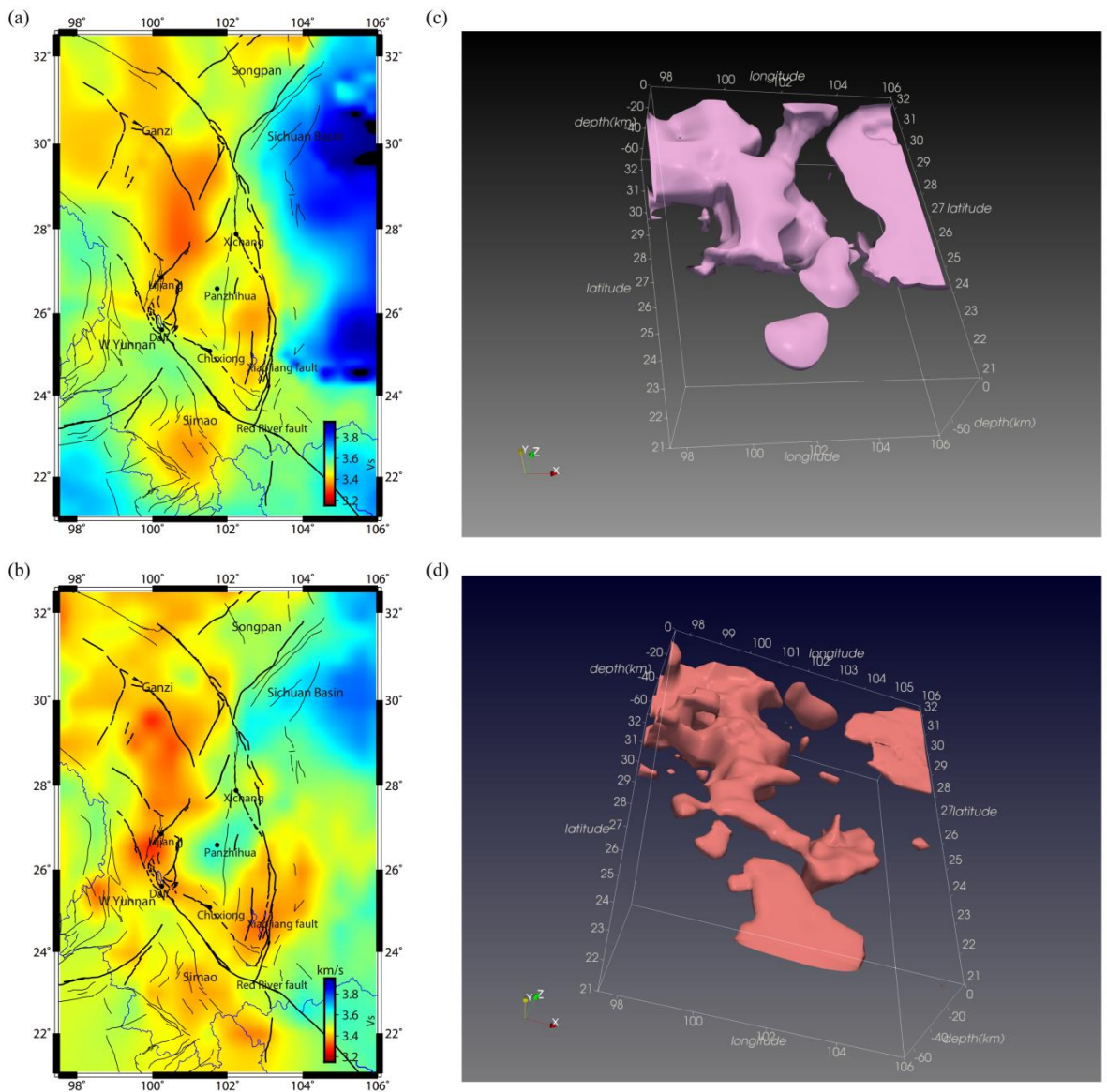
1113   **Figure 5.** S-wave tomography at the depth of 15 km, from Tao et al. (2018) (**a**) and

1114   Shen et al. (2016) (**b**). 3D illustration of crustal LVZs outlined, based on Tao et

1115   al. (2018) (**c**) and Shen et al. (2016) (**d**). The shallow part (~0-10 km) of the low

1116   S-wave velocity zone in the Sichuan Basin is the sediment layer and was

1117   removed in our geodynamic model.

1118
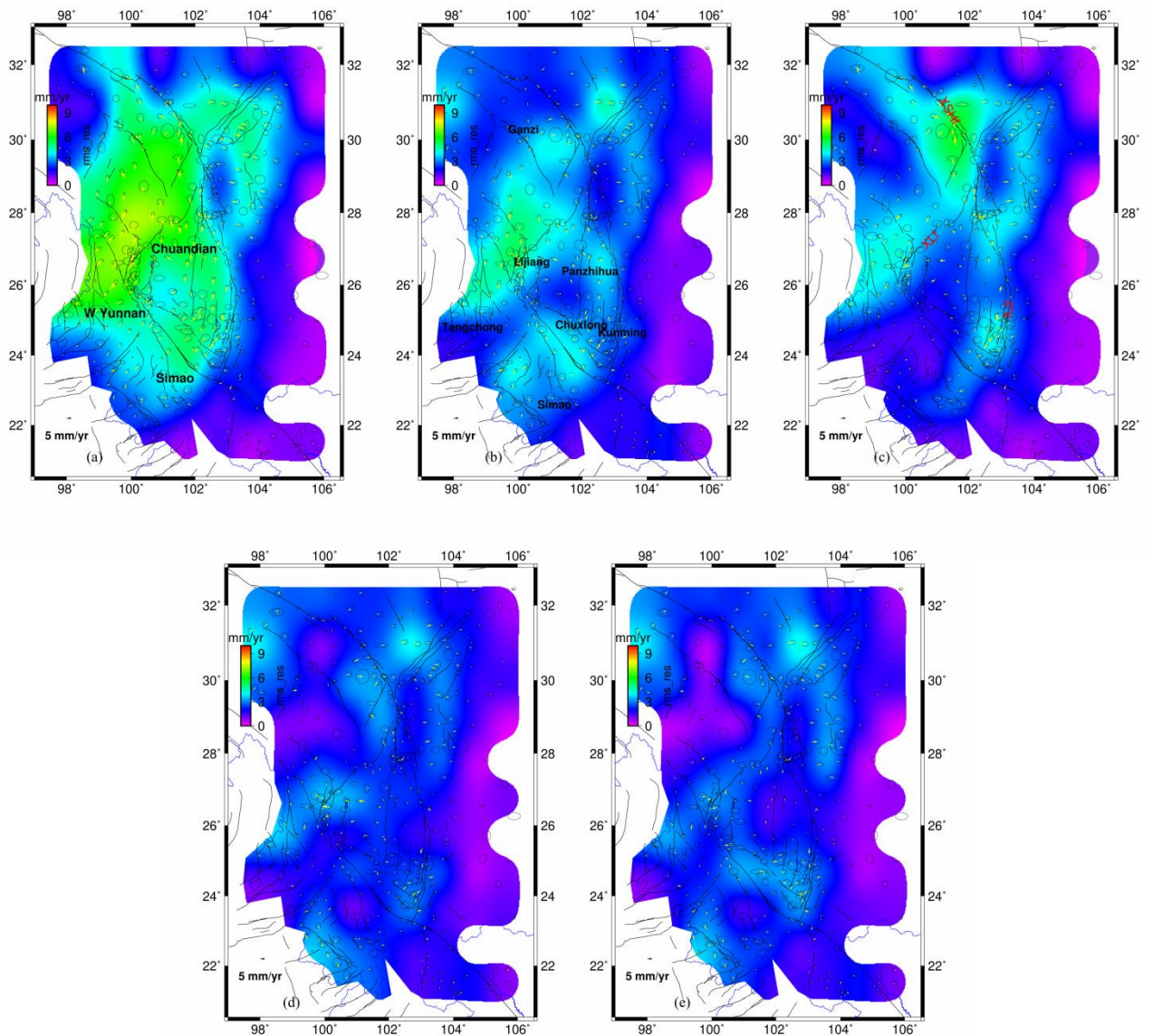
1119   **Figure 6.** Maps of the distribution of the RMS (root mean square) of residual

1120   velocities in SE Tibet resulting from the five models in Table 2. For each GPS

1121   station, the residual velocity (yellow arrows) equals the modeled velocity minus

1122   the observed velocity. The distribution of the scale of residual velocity is

1123   smoothed, mapped, and colored for each figure. (**a**) Model without faults and

1124   LVZs (case_ref); the RMS of the residual velocity is ~4.3 mm/yr. (**b**) Model

1125   with faults (case_fault); the RMS of the residual velocity is ~3.1 mm/yr. The

1126   area with anomalous velocities in (**b**) coincides with the approximate regime of

1127   the LVZs from seismic tomography. (**c**) Model with LVZs only (case_LVZs);

1128   the RMS of the residual velocity is ~3.2 mm/yr. The area with anomalous

1129   velocities in (**c**) coincides with the area of the Xianshuihe-Xiaojiang fault (XSHf

1130   and XJf) and the Xiaojinhe-Lijiang fault (XLf), which have large slip rates. (**d**)

1131   Model with both faults and LVZs (case_both1) based on Tao et al. (2018); the

1132   RMS of the residual velocity is ~2.5 mm/yr. (**e**) Model with both faults and

1133   LVZs (case_both2) based on Shen et al. (2016); the RMS of the residual velocity

1134   is ~2.5 mm/yr.

1135
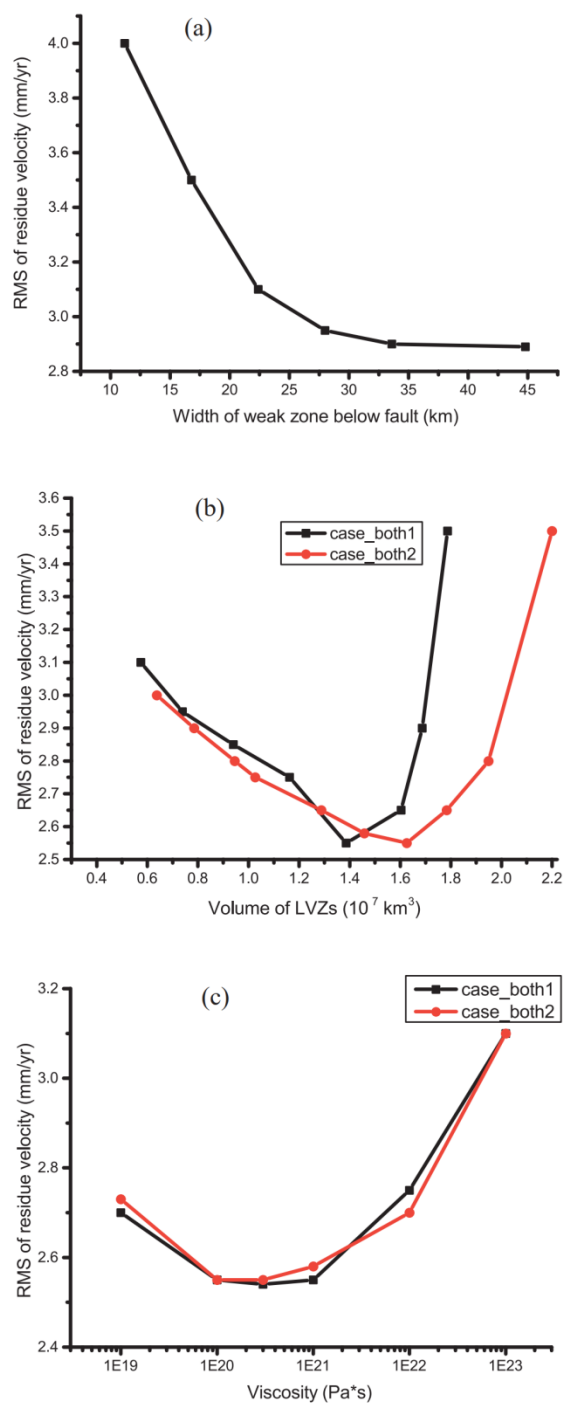
Figure 7. (**a**) RMS of residual velocity vs. the thickness of the lower faulted shear

zones for case_fault. (**b**) RMS of the residual velocity vs. the volume of LVZs

for case_both1 (Tao et al., 2018) and case_both2 (Shen et al., 2016). (**c**) RMS of

residual velocity vs. viscosity of LVZs for case_both1 and case_both2.
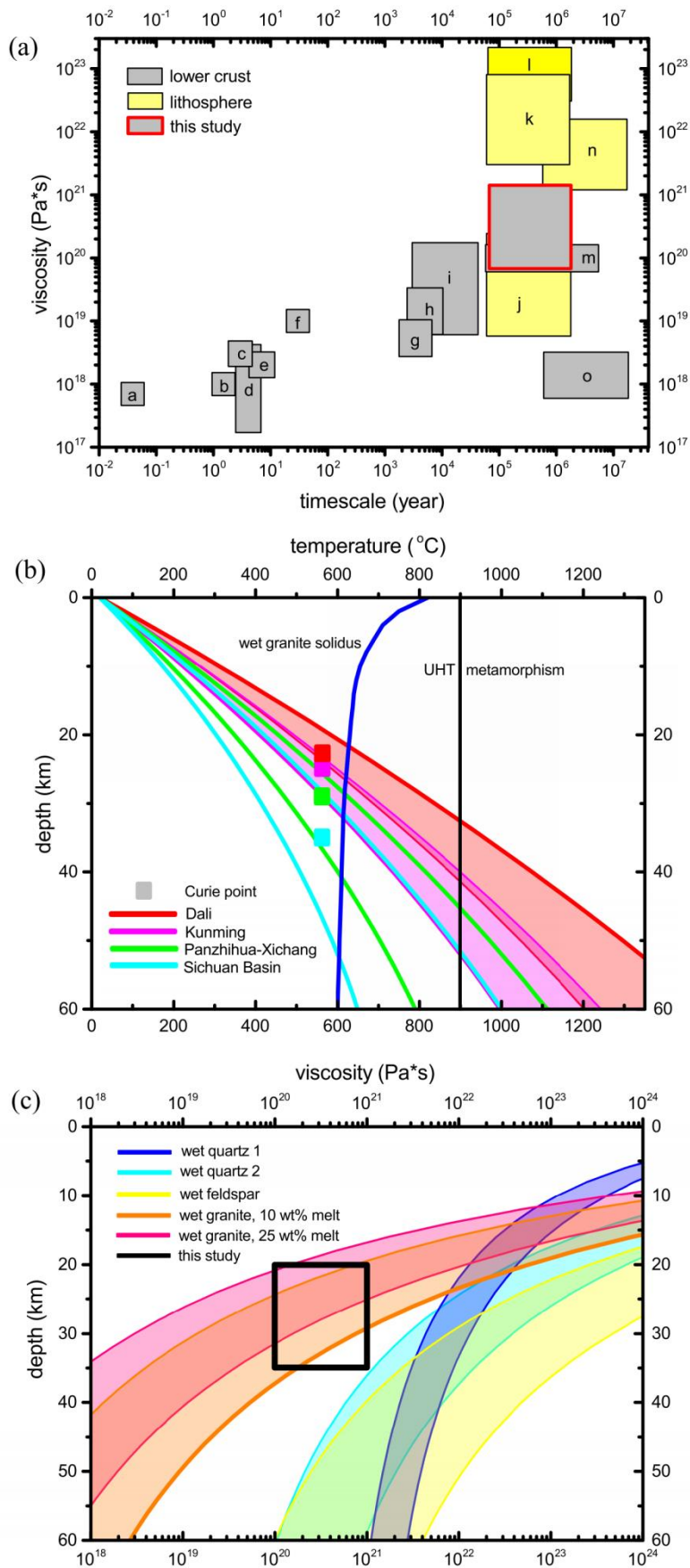
1140
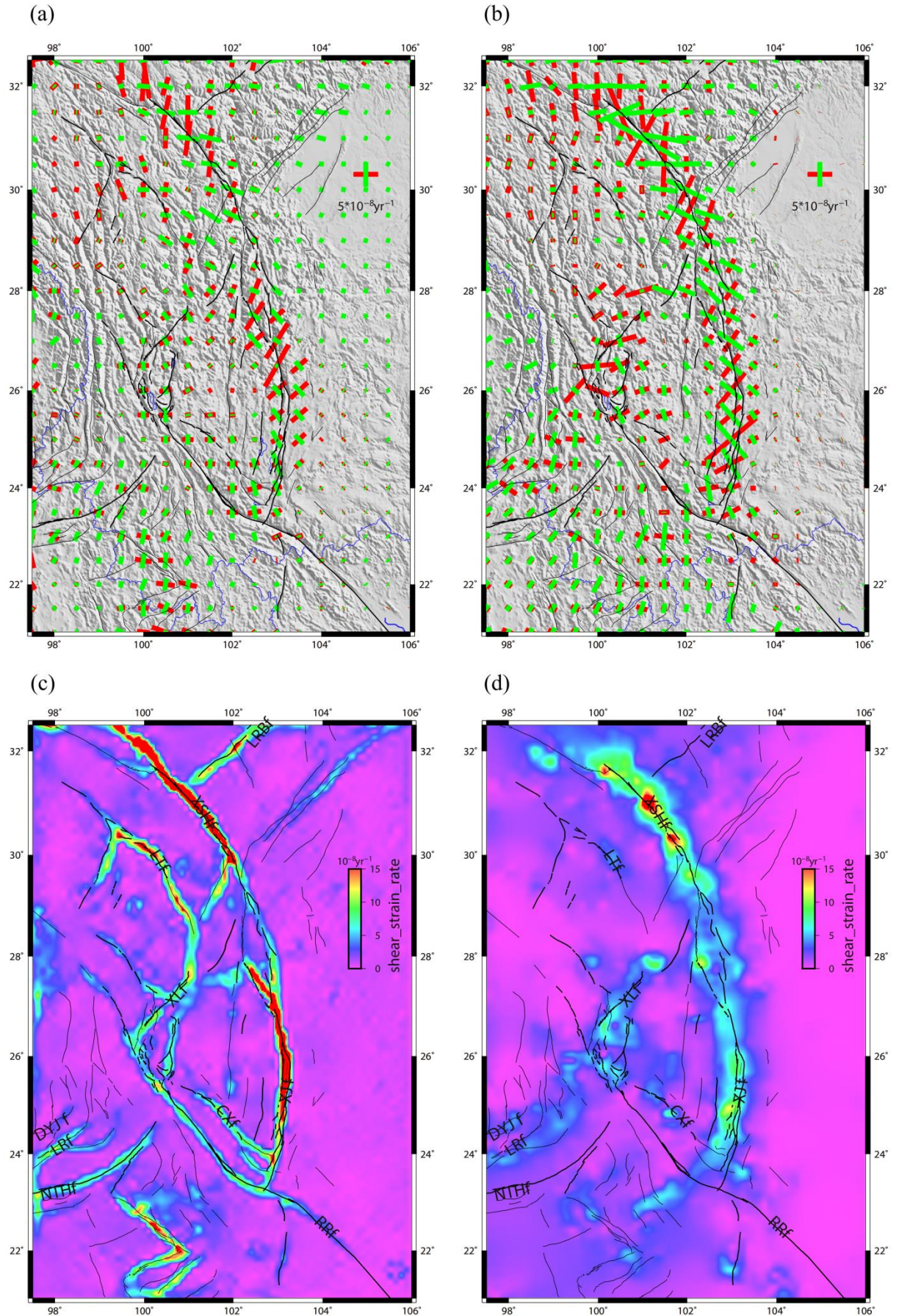
1141 **Figure 8.** Distributions of the strain rate tensor (**a**) and maximum shear strain rate (**c**)

1142 for case_both1 with faults and LVZs; maps of strain rate tensor (**b**) and

1143 maximum shear strain rate (**d**) calculated from smoothed observed GPS data for

1144 SE Tibet (Kreemer et al., 2014). In (**a**) and (**b**), red represents extensional and

1145 green represents compressional strain rate. In (**c**) and (**d**), CXf—Chuxiong fault;

1146 DYJf—Dayingjiang fault; LRf—Longling-Ruili fault; LRBf—Longriba fault;

1147 LTf—Litang fault; NTHf—Nantinghe fault; RRf—Red River fault; XLf—

1148 Xiaojinhe-Lijiang fault; XJf—Xiaojiang fault; XSHf—Xianshuihe fault.
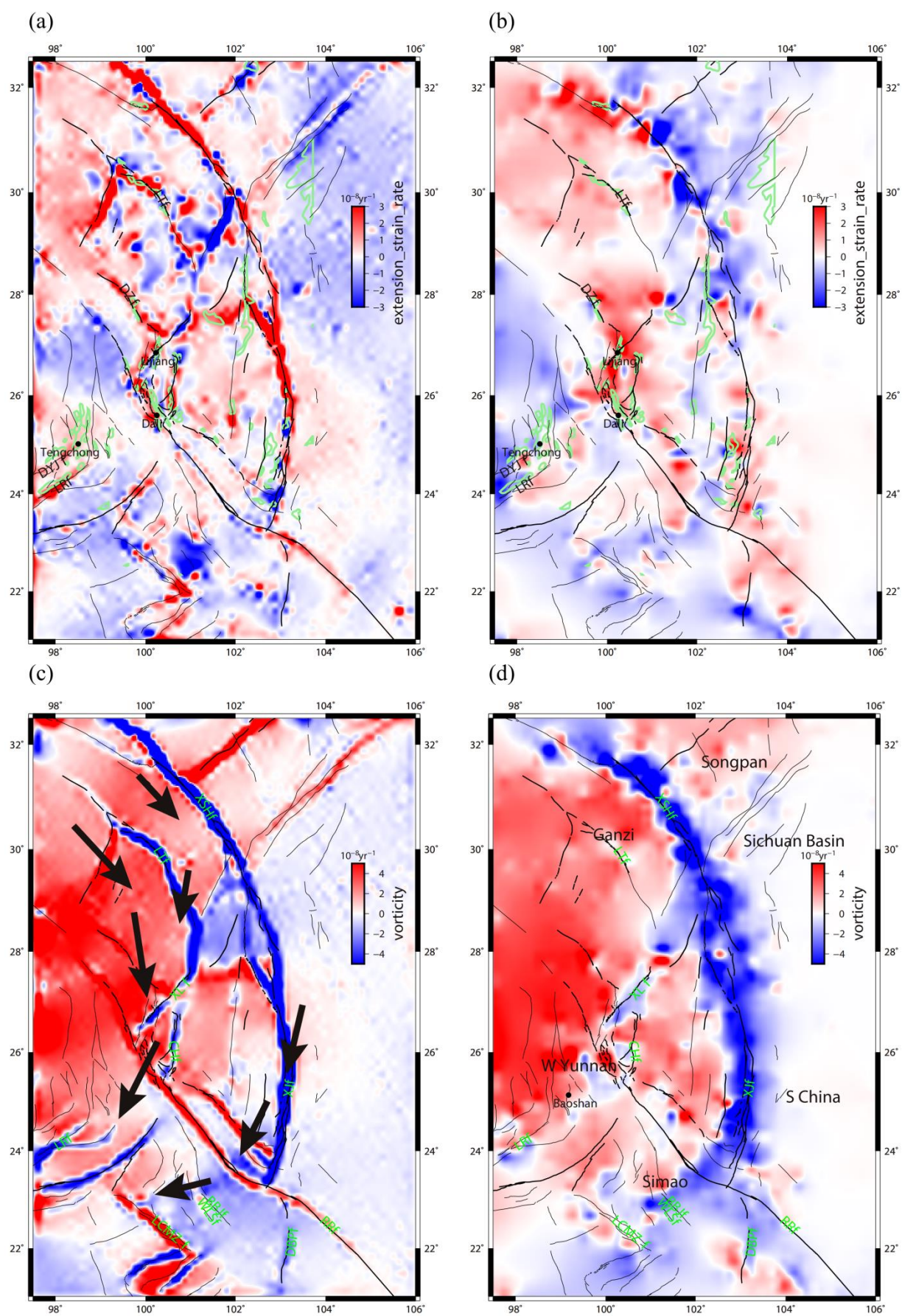
1150   **Figure 9.** Distribution of expansion strain rate (**a**) and vorticity (**c**) for case_both1

1151   with faults and LVZs; maps of expansion strain rate (**b**) and vorticity (**d**)

1152   calculated from smoothed observed GPS data for SE Tibet (Kreemer et al., 2014).

1153   In (**a**) and (**b**), most basins (green outlines; available through http://data.cea-

1154   ies.ac.cn) are under an extensional environment except for the Sichuan Basin

1155   (expansion: red, compression: blue). In (**c**) and (**d**), the strike-slip senses of all

1156   faults agree with geological records (Clockwise/right lateral: red, anti-

1157   clockwise/left lateral: blue). Two channel flows occur in the LVZs, the directions

1158   of which are represented by black arrows. BBJf—Babianjiang fault; CHf—

1159   Chenghai fault; DBPf—Dien Bien Phu fault; DZf—Deqing-Zhongdian fault;

1160   DYJf—Dayingjiang fault; LCMZf—Lancang-Mengzhe fault; LRf—Longling-

1161   Ruili fault; LRBf—Longriba fault; LTf—Litang fault; NTHf—Nantinghe fault;

1162   RRf—Red River fault; WLSf—Wuliangshan fault; XLf—Xiaojinhe-Lijiang fault;

1163   XJf—Xiaojiang fault; XSHf—Xianshuihe fault.

1165 **Figure 10.** (**a**) Viscosity of mid-lower crust (gray) or entire lithosphere (yellow) in SE

1166 Tibet constrained by previous geodynamic modeling over different timescales

1167 (based on Huang et al. (2014) and Panda et al. (2019)). Postseismic: a-Shao et al.

1168 (2011); b-Huang et al. (2014); c-Xu et al. (2014); d-Wang et al. (2019); e-Diao et

1169 al. (2018); f-Zhang et al. (2009); Earthquake cycle: g-Zhu & Zhang (2013);

1170 Lake-shoreline rebound: h-Shi et al. (2015); i-England et al. (2013); Geodynamic:

1171 j-Yin & Taylor (2011); k-Flesch et al. (2001); l-Panda et al. (2019); m-Bischoff

1172 & Flesch (2018); Topographic: n-Jiménez-Munt & Platt (2006); o-Clark &

1173 Royden (2000) and Xu et al. (2016). (**b**) Temperature profiles for the area with

1174 LVZs (Kunming and Dali) and without LVZs (the Sichuan Basin and Panzhihua-

1175 Xichang). Squares indicate the depth of the Curie surface (Gao et al., 2015). Thin

1176 light blue and black lines represent curves of wet granite solidus and ultrahigh

1177 temperature metamorphism, respectively. (**c**) Viscosity profiles based on the

1178 temperature of two LVZs from the temperature profiles (**b**), of wet quartzite

1179 (deep blue/wet quartz 1: Hirth et al., 2001; light blue/wet quartz 2: Rutter &

1180 Brodie, 2004), wet feldspar (yellow: Rybacki et al., 2006), and partially molten

1181 wet granite (Rutter et al., 2006) with a melt fraction of 10wt% (orange) and 25wt%

1182 (pink). Nonlinear flow laws are used and the reference strain rate is 1×10^{-15} s^{-1}.

1183

1184

1185

1186

1187   **Table 1.** Constants used in the model.

X length	1294 km
Y width	884 km
Z depth	302 km
D_{air} air layer thickness	20 km
G shear modulus	3×10^{10} Pa
Ra Rayleigh number	5×10^{7}
α thermal expansion coefficient	3×10^{-5} K^{-1}
η_0 reference mantle viscosity	1×10^{19} Pa·s
κ_0 reference thermal diffusivity	1×10^{-6} W/m·K
C_0 initial plastic yield stress	40 MPa
C_f minimum plastic yield stress	0.6 MPa
ε_f reference plastic strain	0.3
T_0 reference temperature	1500 K
R gas constant	8.31 J·K^{-1} mol^{-1}
E activation energy	540 kJ/mol
μ coefficient of friction	0.5
n strain exponent	3.5
$\dot{\varepsilon}_0$ reference strain rate	1×10^{-15} s^{-1}

1188

1189   **Table 2.** Cases in Figure 6 and parameters used in these cases.

Name	Fault included	LVZs included	LVZs model	thickness of weak zone below the fault (km)	Ratio r of LVZs	Viscosity of LVZs (Pa·s)	RMS of residual velocity (mm/yr)
case_ref	no	no					~4.3
case_fault	yes	no		22			~3.1
case_LVZs	no	yes	Tao_2018		0.7	10^{20}	~3.2
case_both1	yes	yes	Tao_2018	22	0.7	10^{20}	~2.5
case_both2	yes	yes	Shen_2016	22	0.4	10^{20}	~2.5

1190